JACS Au
AN OPEN ACCESS JOURNAL OF THE AMERICAN CHEMICAL SOCIETY

Tuning Solid Electrolyte Interphase Formation before Plating Onset in Anode-Free Sodium Batteries

Published as part of JACS Au special issue "Future Perspectives on Battery Chemistries".

Aaron M. Melemed, Sungil Hong, Jonathan R. Thurston, Alexis Luglio, Ethan B. Rose, Thomas S. Marchese, Jianwei Lai, Ethan J. Crumlin, Ying Shirley Meng, Nirala Singh, Rajeev S. Assary, and Neil P. Dasgupta*

Cite This: https://doi.org/10.1021/jacsau.6c00193

Read Online

ACCESS | Metrics & More | Article Recommendations | Supporting Information

ABSTRACT: Sodium (Na) batteries are of growing interest due to the higher earth abundance of sodium than lithium, as well as their promising theoretical energy density when metallic Na anodes are used. However, Na plating and stripping are heavily influenced by the physicochemical properties of the solid electrolyte interphase (SEI), which is directly influenced by the solvent and salt used for the electrolyte. While most studies focus on the SEI that forms on the surface of Na metal after plating, we expand this analysis by identifying a nanoscale "pre-plating" SEI that forms on the current collector (CC) prior to the onset of Na plating. Here, we systematically investigate an array of Na salt and glyme solvents in the electrolyte and determine the associated impacts on pre-plating SEI formation on aluminum CCs. By combining analytical electrochemistry approaches with a multimodal suite of spectroscopy techniques (X-ray, infrared, and Raman), supported by density functional theory calculations, we reveal a direct correlation between the Na^+ coordination environment and pre-plating SEI composition. We find that longer-chain glymes produce larger proportions of organic alkoxide products in the interphase, consistent with increased Na^+−glyme interactions, while the fraction of salt-derived inorganic products (e.g., NaF) correlates with Na^+−anion coordination. These insights highlight the critical influence of electrolyte composition—particularly solvent identity and Na^+ coordination—on the initial SEI formation in anode-free Na batteries.

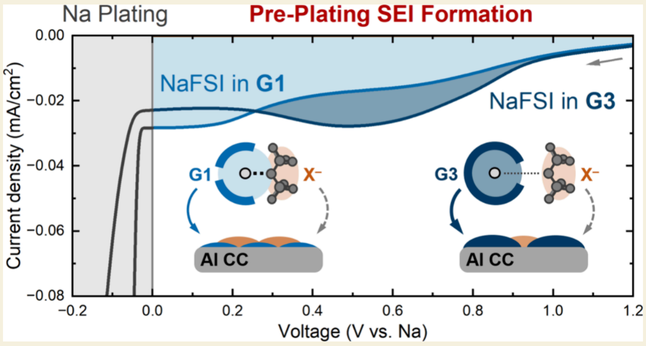

KEYWORDS: *sodium metal anode, anode-free batteries, electrolyte coordination, solid electrolyte interphase, surface chemistry*

INTRODUCTION

Given concerns surrounding the earth abundance and supply chain vulnerability of lithium (Li) in Li-ion batteries, there is growing interest in developing rechargeable batteries that use more sustainable and geographically distributed materials, while still enabling comparable energy density. Batteries based on sodium (Na) are a compelling alternative due to the ~1000-fold higher concentration of Na in the earth's crust. Na metal anodes have a reasonably high theoretical specific capacity (1166 mAh/g, 1128 mAh/cm^3), in comparison to graphite anodes in Li-ion batteries (372 mAh/g, 818 mAh/cm^3) and Li metal anodes (3860 mAh/g, 2060 mAh/cm^3).[1−3] A major challenge with the use of Na metal, however, is the higher chemical reactivity compared to Li, which leads to poor reversibility in conventional carbonate-based battery electrolytes and has hindered Na battery development until the past decade.[4−6] In 2015, Seh et al. reported Na plating/stripping with ~99.9% Coulombic efficiency (CE) using $NaPF_6$ in glymes[6]—a reversibility benchmark that has been decades in the making for Li metal anodes.[7]

The two most prominent mechanisms of Coulombic inefficiency in Li systems are the formation of inactive "dead" Li, in which the loss of physical and/or electrical contact between plated Li and the current collector (CC) prevents Li stripping,[8,9] and the formation of a solid electrolyte interphase (SEI), which modulates Li electrochemistry at the electrode/electrolyte interface. SEI formation accounts for the majority of capacity loss in highly reversible Li systems ($\gtrsim$95% CE).[10] In these systems, the formation of a highly functional SEI enables relatively homogeneous Li plating/stripping that in

Received: February 6, 2026
Revised: May 12, 2026
Accepted: May 13, 2026

turn decreases the likelihood of electronically isolated Li deposits. The same two mechanisms of capacity loss are typically proposed for Na metal anodes. Consistent with this understanding, the high CE of the $NaPF_6$/glyme systems compared to other solvents has been attributed to the formation of a compact, inorganic-rich SEI on the surface of the plated Na.[6,11] It is therefore of critical interest to deepen our fundamental understanding of the relationships between electrolyte formulation and the resulting SEI chemistry in highly reversible Na electrolyte systems.

Recent studies have explored Na SEI in other glyme-based systems, similarly reporting high reversibility using the salts $NaBF_4$,[12] NaOTf,[13] highly concentrated NaFSI,[14−17] and even the fluorine-free $NaBPh_4$.[18] The SEI layers in these systems have also been observed to exhibit an inorganic-rich composition (typically dominated by NaF and/or Na_2O). Given these compositional trends, as well as the reported thermodynamic and electrochemical stability of glymes[19,20] compared to carbonates, glyme solvents are typically thought to play a supporting role. It has been proposed that weaker Na^+−solvent interactions allow for a relative increase in Na^+−anion coordination, resulting in an increase in the amount of salt-derived SEI phases.[21−23] However, decoupling the roles of the solvent and salt in SEI formation—which involve multiple different reaction pathways—is less well understood for Na electrolytes. The composition and role of solvent-derived organic phases in the SEI, in particular, warrants further investigation.

Another important aspect of Na electrochemistry is the physicochemical environment of the CC surface before plating onset, which governs the early stages of nucleation and growth during the first formation cycle of the battery. This is particularly important in "anode-free" configurations—which maximize theoretical energy density—where the initial nucleation processes occur on a heterogeneous metal surface.[24] In Li metal systems, for example, wetting behavior,[25] electrical resistance[26] and chemical inhomogeneity[24] of the CC surface can cause current focusing during Li nucleation, intensifying the heterogeneity of Li deposits and hindering extended cycling performance. The native oxide species that are inevitably present on the surface of Cu CCs have also been found to chemically react with plated Li,[27] which can influence nucleation behavior. Not only is the CC surface before cell construction important, but the formation charging protocols at potentials above 0 V vs the Li electrode have also been found to promote electrolyte decomposition and alter the surface composition, resulting in the formation of an SEI layer before the onset of Li plating.[28] Similarly, electrolyte decomposition has also been observed in Na-based electrolytes on the surface of a Cu CC.[29,30] Recently, Dettmann et al. observed that substrate composition (Cu, glassy carbon, and silicon) impacts the decomposition of both Li- and Na-based carbonate electrolytes ($LiPF_6$ and $NaPF_6$ in ethylene carbonate) at their respective positive potentials, leading to different interfacial compositions.[31]

Motivated by these previous studies, the goal of this work is to deepen our understanding of the various factors that influence SEI formation on the CC surface in anode-free Na systems. We selected Al as the CC material, given its technological relevance and increasing use in anode-free Na batteries as an alternative to Cu. This use is motivated by the higher earth abundance (and lower cost) of Al, lower density of Al (which reduces battery weight), and lack of alloying behavior with Na.[2,32−34] In this study, we systematically examine various Na salts and glyme solvents to explore the relationship between the Na^+ coordination environment in the electrolyte and SEI composition at "pre-plating" (positive) potentials.

The electrolytes examined are conventional Na battery salts ($NaPF_6$, $NaBF_4$, NaFSI, NaOTf, and NaTFSI) in glymes of increasing lengths (G1 (1,2-dimethoxyethane), G2 (bis(2-methoxyethyl) ether), G3 (triethylene glycol dimethyl ether), and G4 (tetraethylene glycol dimethyl ether)). Electrochemical measurements in anode-free Na−Al cells reveal irreversible reductive capacities before the onset of Na plating in each electrolyte. Compositional analysis reveals the presence of both anion and solvent decomposition products on the CC surface, providing evidence of a pre-plating SEI. The composition of this interphase is dependent on both electrolyte composition and polarization potential, which suggests competition between multiple electrolyte decomposition pathways. Spectroscopic measurements further demonstrate a correlation between Na^+−glyme coordination and solvent-derived alkoxide products in the pre-plating SEI, which is further investigated by ab initio simulations. This work emphasizes the impact that electrolyte composition can have on the early stages of battery operation, enabling a more complete understanding of the relationships between electrolyte composition, SEI formation, and surface chemistry of the CC in anode-free systems.

EXPERIMENTAL METHODS

Materials Preparation

All electrolyte preparation was conducted inside an argon (Ar) glovebox (O_2 content < 0.5 ppm, H_2O content < 0.5 ppm) with a standalone solvent trap. All solvents were dried over activated molecular sieves for at least 72 h; the water content for each solvent was determined to be <10 ppm by Karl Fischer (KF) titration. All salts were vacuum-dried at 100 °C overnight. One mol of salt was used per 1 L of solvent, unless the salt was partially soluble or insoluble. Battery-grade Na metal chips were used as-received. Manually prepared Na foil electrodes were cut and rolled from a Na ingot in the Ar glovebox. Al and Cu foil CCs were punched, cleaned, and vacuum-dried overnight at 60 °C. Celgard 2325 was vacuum-dried overnight at 60 °C for the separator. All other coin cell components were sonicated and vacuum-dried overnight at 60 °C.

Electrochemical Characterization

"Anode-free" Na−Al coin cells were constructed inside the Ar glovebox and crimped at 1200 psi. Na−Al cells were utilized for all electrochemical measurements; voltages are plotted with respect to the Na electrode. A Bio-Logic potentiostat was used for linear sweep voltammetry (LSV), cyclic voltammetry (CV), galvanostatic reduction, and potential hold experiments. All electrochemistry was performed at 30 °C. Ionic conductivity measurements were performed inside the Ar glovebox with a conductivity probe. The probe was immersed in 10 mL of electrolyte until a steady reading was obtained. Three readings were acquired per electrolyte.

Materials Characterization

All CC samples were rinsed with G1 and vacuum-dried at room temperature inside the Ar glovebox. Samples were hermetically sealed for transfer to their respective analysis machines. Attenuated total reflectance Fourier transform infrared spectroscopy (ATR-FTIR) measurements were performed under ambient air conditions, utilizing a spectral resolution of 4 cm^{-1} and an averaged accumulation of 64 scans with background subtraction. X-ray photoelectron spectroscopy (XPS) samples were mounted to the sample stage in another Ar glovebox and transferred to the XPS chamber without air exposure. High-resolution spectra were calibrated to the adventitious carbon

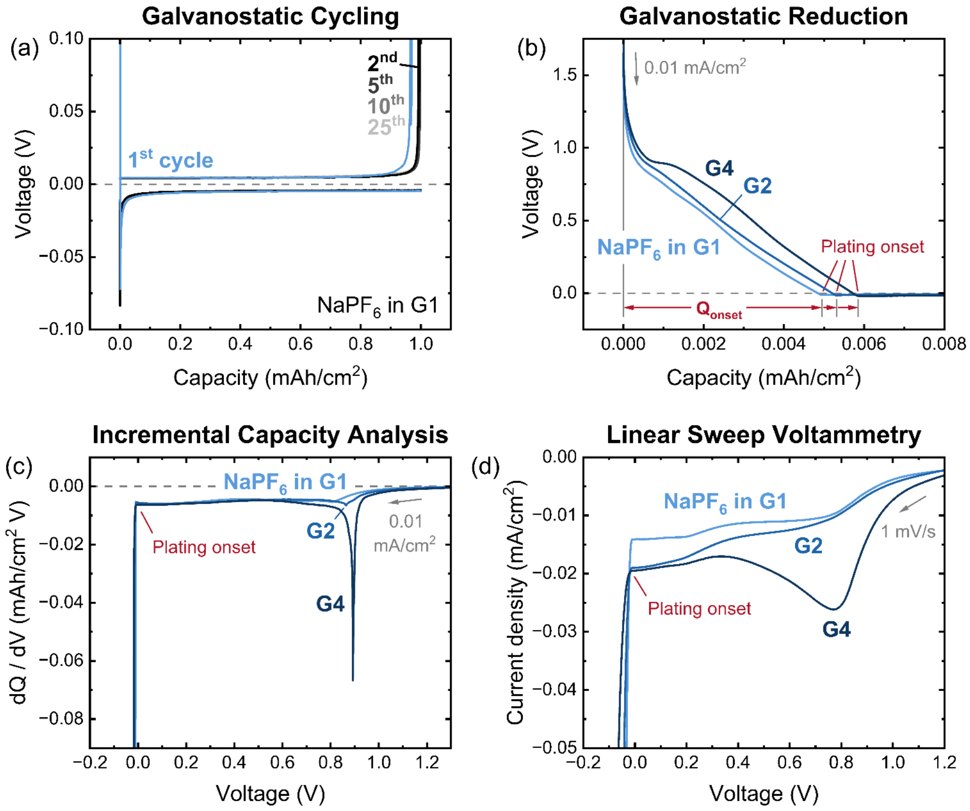

Figure 1. Reduction behavior of $NaPF_6$ in glyme electrolytes onto Al current collectors. (a) 25 galvanostatic Na plating/stripping cycles of $NaPF_6$ in G1 at 0.5 mA/cm^2, to 1 mAh/cm^2, with a 1 V cutoff during stripping. (b) Initial galvanostatic reduction and (c) the resulting incremental capacity analysis of $NaPF_6$ in G1, G2, and G4 onto Al at 0.01 mA/cm^2. (d) Initial linear sweep voltammetry from OCV to plating onset performed at 1 mV/s. Each curve corresponds to one sample obtained in a Na−Al coin cell, where Al is the working electrode and Na is the reference/counter electrode.

peak at 284.8 eV, fit using CasaXPS, and background-subtracted for data presentation. Scanning electron microscopy (SEM) samples were double-sealed under Ar and shipped to Argonne National Lab for analysis. Samples were mounted on SEM stubs in another Ar glovebox and transferred to a plasma focused ion beam (PFIB) SEM dual-beam system for imaging in an airtight transfer system under Ar. Stitched micrographs of Al CCs were acquired and used to select representative regions for X-ray energy dispersive spectroscopy (EDS) mapping. Electrolyte samples for Raman spectroscopy were placed inside glass tubes and sealed inside the Ar glovebox. Raman spectroscopy was performed on the sealed samples using a 785 nm laser. Raman spectra underwent peak deconvolution and background subtraction for data presentation. Additional experimental details such as product and vendor information, sample preparation procedures, and analysis parameters are included in the Supporting Information.

COMPUTATIONAL METHODS

Density functional theory (DFT) calculations were carried out using the Gaussian 16 software package[35] at the ωB97X-D level of theory[36] coupled with the 6−31+G(d,p) Pople basis set.[37,38] Solvation effects using the Polarizable Continuum Model (PCM)[39,40] as implemented in Gaussian, where dielectric constants ε = 7.54, 7.363, 7.578, and 7.79 were used for G1, G2, G3, and G4, respectively.[41] Vibrational frequency calculations were performed to confirm that the optimized structures are local minima of the potential energy surfaces by the absence of imaginary frequencies. Small imaginary frequencies (<10 cm^{-1}) were ignored. The Gibbs free energies (G) were calculated assuming standard conditions, 25 °C and 1 atm.

Classical molecular dynamics (MD) simulations of NaFSI in G1−G4 were performed using GROMACS[42] with the OPLS-AA force field.[43,44] Coordination environments and ion-pair populations (aggregate, AGG; contact ion pair, CIP; solvent-separated ion pair, SSIP) were analyzed from isothermal−isobaric (NPT) ensemble trajectories at 298.15 K and 1 bar. Additional computational details[45−59] are included in the Supporting Information.

RESULTS AND DISCUSSION

Electrochemical Behavior before the Onset of Na Plating

Figure 1a shows the voltage traces during galvanostatic plating and stripping of Na onto an Al CC for an electrolyte composed of $NaPF_6$ in G1, using the same electrolyte and cycling conditions as Seh et al. (0.5 mA/cm^2, 1 mAh/cm^2, 1 V cutoff).[6] While we observed a high average CE of 99.7% for cycles 2 through 25, the CE of the first cycle (light blue trace) was noticeably lower at 97.8% (Figure S1 in the Supporting Information). These trends are consistent with the CE data reported by Seh et al.[6] In this study, we observed a first cycle capacity loss of ∼0.02 mAh/cm^2. However, not all of this capacity loss can be attributed to chemical reactions between plated Na metal and the electrolyte—we observed a small but reproducible amount of reductive capacity before the onset of Na plating in the first cycle (∼0.001 mAh/cm^2, as shown in Figure S2). We define the areal charge passed before the nucleation of plated Na as Q_{onset}, as has been previously defined in anode-free Li systems.[60] The magnitude of Q_{onset} increased with lower galvanostatic current densities (Figure S2), reaching ∼0.005 mAh/cm^2 at a current density of 0.01 mA/cm^2. At lower current densities, the voltage vs capacity curves of Figure S2 deviated from linear capacitive behavior to greater extents, indicating an increase in Faradaic reactions at the CC (likely attributed to SEI formation) enabled at slower

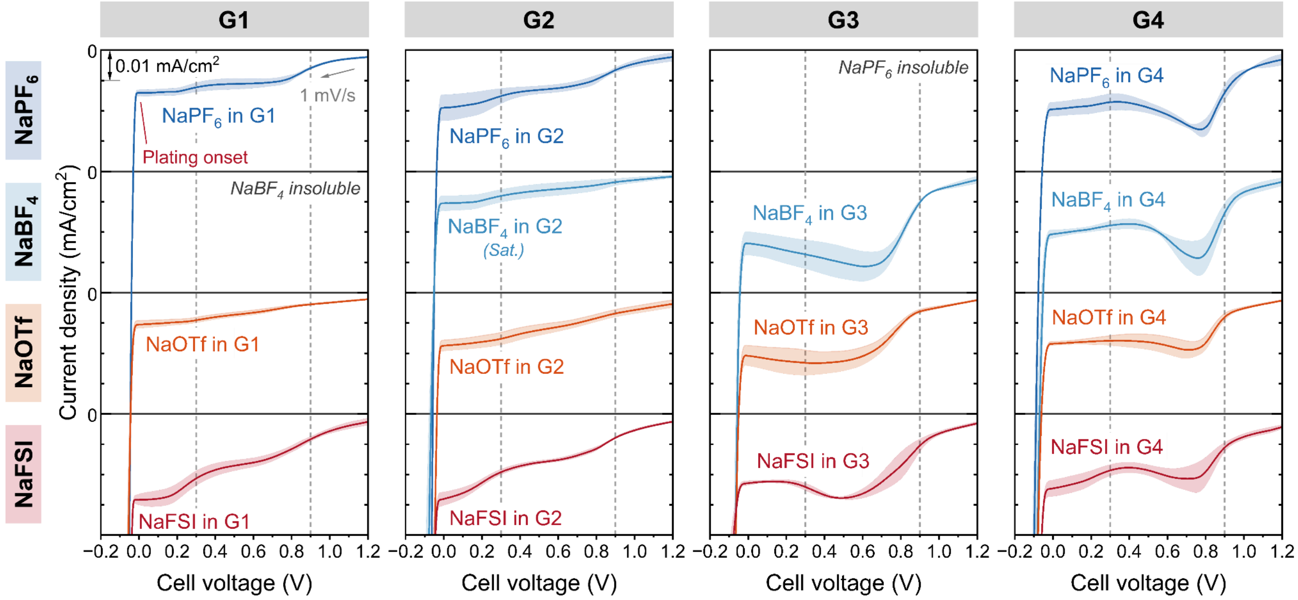

Figure 2. Linear sweep voltammetry of a range of Na-based electrolytes. LSV at 1 mV/s was performed from OCV to Na plating. The salts used were $NaPF_6$, $NaBF_4$, NaOTf, and NaFSI, with concentrations of 1 mol per $L_{solvent}$ unless saturated (as for $NaBF_4$ in G2) or insoluble. Solvents used were G1, G2, G3, and G4 as noted above each column. Each curve corresponds to the average of three samples, with the surrounding shaded area corresponding to one standard deviation. Curves are offset for clarity, with grid lines corresponding to 0 mA/cm^2 and a scale bar of 0.01 mA/cm^2. Vertical dotted lines provide a visual guide to the electrochemical features at 0.3 and 0.9 V.

time scales. Therefore, in this study we focus on the lowest current density conditions (0.01 mA/cm^2) to provide sufficient time to probe these initial Faradaic reactions prior to the onset of Na deposition.

We next varied glyme chain length in the electrolyte to examine the impact of electrolyte chemistry on pre-plating reduction. Figure 1b shows the galvanostatic reduction of $NaPF_6$ in G1 (light blue trace), G2 (blue), and G4 (dark blue) onto an Al CC. ($NaPF_6$ was insoluble in G3). We observed a monotonic increase in Q_{onset} as the glyme chain length increased. We also observed a difference in the voltage trace shape, where a plateau emerged around 0.9 V for the longer glymes, which appeared to account for the higher value of Q_{onset}. To quantify these differences, an incremental capacity (dQ/dV) curve is plotted in Figure 1c. The peak at 0.9 V, which increases in magnitude from G1 to G4, suggests that a distinct Faradaic reduction reaction is occurring at this potential.

Linear sweep voltammetry (LSV) was performed with the same electrolyte formulations to better probe the reaction dynamics. Figure 1d shows the LSV traces swept from open circuit voltage (OCV, typically >1.5 V) to the onset of plating at a scan rate of 1 mV/s. This scan rate was chosen to provide similar time scales to the ~0.01 mA/cm^2 galvanostatic reduction experiments. Along with the previously identified peak beginning at ~0.9 V, the LSV revealed an additional reductive feature beginning at ~0.3 V. The potentials of these reduction peaks observed herein are similar to those reported by Dettmann et al. from LSV (10 mV/s) of $NaPF_6$ in ethylene carbonate onto Cu (~0.8 V) and glassy carbon (~0.25 V), which the authors attributed to electrolyte decomposition.[31] We compared LSV on two other CCs (Cu and stainless steel, Figure S3) and observed reductive features at both ~0.9 and ~0.3 V regardless of substrate; we thus similarly conclude this electrochemical behavior corresponds to electrolyte decomposition. There were slight differences in the relative current densities of the two reductive reactions (i.e., the LSV curve shapes) for the different CCs (Figure S3), which suggest some degree of substrate dependence. This is to be expected, as a range of chemical and structural interactions along the electrolyte−substrate interface will impact the associated reaction pathways.[24]

To examine the influence of using nonether solvents, we also performed LSV experiments with $NaPF_6$ in a series of carbonate-based solvents onto Al (Figure S4). The LSV of the carbonates similarly exhibited reductive features. The presence of these two reductive peaks in both ethers and carbonates—solvents with different functional groups and decomposition pathways—indicates that the reductive processes at these potentials are associated with common constituents, such as the salt species (Na^+ and/or PF_6^-) or any shared electrolyte impurities, not just the solvent. However, the reductive features were shifted to more cathodic potentials (by ~0.1 V) in carbonates compared to the glyme-based electrolytes (Figure 1d), which suggests that the reaction thermodynamics are impacted by solvation.[61] Additionally, the differences in current density of the 0.9 V peaks observed with different glymes (Figure 1d), which have relatively similar Guttmann donor and acceptor numbers,[62] suggest that the solvent also impacts electrochemical reaction dynamics (i.e., transport and/or kinetics). We note that these effects do not preclude decomposition pathways involving the solvent, which we will discuss in the following sections.

To further examine the role of salt and solvent species on these pre-plating reduction reactions, we performed a systematic study of various electrolyte compositions. Salt and solvent were independently varied while the concentration was held constant at 1 mol per $L_{solvent}$. Figure 2 shows an array of LSV curves, where the columns represent the different solvents (G1 through G4), and the rows represent different fluorinated salts ($NaPF_6$, $NaBF_4$, NaOTf, and NaFSI). Further quantitative analysis of the LSV curves is available in Figures S5−S7.

https://doi.org/10.1021/jacsau.6c00193

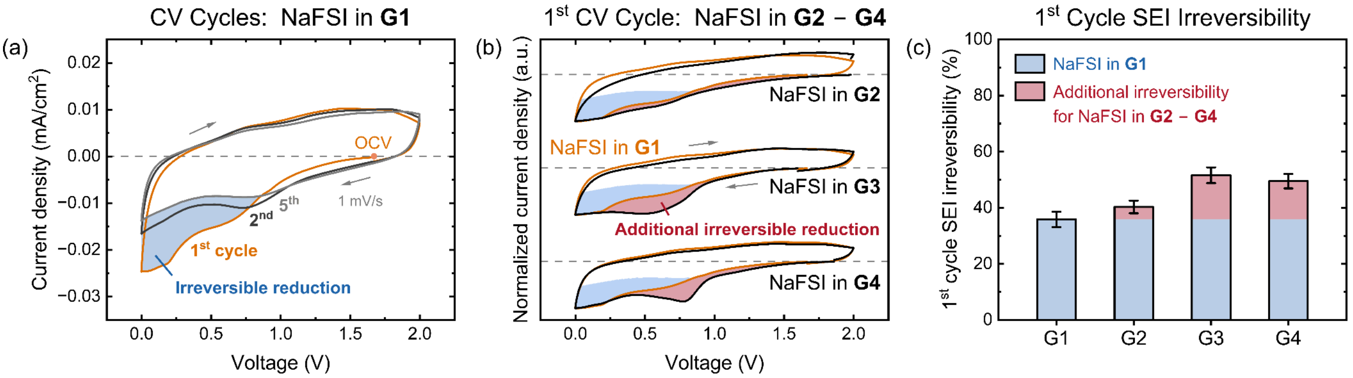

Figure 3. Cyclic voltammetry of NaFSI in glymes. (a) The 1st, 2nd, and 5th CV cycles of one representative cell containing NaFSI in G1 at a scan rate of 1 mV/s. The blue shaded area is a visual guide that demonstrates current density associated with irreversible reduction. (b) The 1st CV cycle (black) of one cell containing NaFSI in G2, G3, or G4 overlaying the 1st CV cycle of NaFSI in G1 (orange) from (a). Current density is normalized to each cell's respective value at 0 V for comparison purposes, with the dotted lines indicating 0 mA/cm^2. The red shaded areas demonstrate additional irreversible current density compared to the G1-based electrolyte. (c) Percent of irreversible charge passed during the 1st CV cycle. The red area again corresponds to additional irreversible capacity compared to the G1-based electrolyte. The average value for three cells is shown for each electrolyte, with error bars corresponding to one standard deviation.

Broadly speaking, the LSV curves within a specific column (i.e., using different salts but the same solvent) exhibited the same general shape. This further suggests that these reductive processes are associated with the Na$^+$ cation and/or an anion-derived fluoride (the only other common salt moiety among the four anions).

We observed clear differences in electrochemical behavior across the columns of Figure 2 as the glyme chain length increased. Most notably, the LSV curves for the G3 and G4 electrolytes exhibited a dominant peak near 0.5−0.8 V, in contrast to the two distinct electrochemical features of the G1 and G2 electrolytes. The broad reduction peak overshadowed the expected feature at 0.3 V for the G3 electrolytes. We investigated whether this peak might be convoluting other reduction processes in this potential window or might reflect a change in reaction potential for the longer glymes. The NaFSI electrolytes were chosen as a case study, given the solubility of the salt in all four glymes. Galvanostatic reduction and dQ/dV of NaFSI in G1−G4 (Figure S8) displayed the same prominent voltage plateau near 0.9 V for all four glymes, as well as the smaller characteristic reductive feature at 0.3 V. Therefore, we could confirm that the different LSV curve shapes of Figure 2 reflected different reaction dynamics of the same pair of electrochemical reactions—with the reaction at 0.9 V in particular facilitated in the G3 and G4 electrolytes.

As an additional case study, we examined the electrochemical behavior of another common fluorinated salt, NaTFSI. In contrast to the other anions, which have been broadly reported to enable high CE values during Na plating/stripping in a variety of electrolyte configurations,[6,11−17] NaTFSI-based electrolytes are reported to be irreversible.[6,14] Interestingly, the LSV of NaTFSI in G1−G4 (Figure S9) exhibited significant differences to those of the other anions. We did not observe the distinct electrochemical feature near 0.9 V for any of the four NaTFSI-based electrolytes, though a smaller amount of reductive current density was still observed. This further suggests that the prominent Faradaic reaction at 0.9 V is dependent on anion chemistry, as discussed in the Supplementary Analysis section of the Supporting Information. Despite the absence of the 0.9 V feature, the reductive features at 0.3 V were still present (though slightly suppressed) in the NaTFSI electrolytes. The lower-potential reaction is therefore not inherently coupled to the 0.9 V reaction. We next investigated whether these Faradaic reactions constituted irreversible electrolyte decomposition.

The irreversibility of the pre-plating reduction reactions was observed using cyclic voltammetry (CV), with NaFSI in G1 again as the model system. A potential window between 0 and 2 V was chosen to avoid Na plating, while also providing a sufficient positive potential to probe the reaction at 0.9 V. Figure 3a shows the first, second, and fifth CV cycle of NaFSI in G1 onto Al. The first cycle exhibited a clear asymmetry in current density, with a greater magnitude in the reductive current compared to the oxidative current. The oxidative current density exhibited a somewhat flat profile that indicates the presence of capacitive and/or pseudocapacitive effects.[63] These effects are further evident through rate-dependent CV sweeps for a representative electrolyte in Figure S10. Notably, the majority of the irreversible reductive capacity occurred during the first cycle (Figure 3a), as the second and fifth cycles essentially overlaid during both reduction and oxidation.

The blue shaded area in Figure 3a provides a visual guide for this first cycle irreversibility. The irreversible charge was observed to primarily occur within the potential range of 0−0.9 V, indicating that the 0.3 and 0.9 V reduction reactions are associated with irreversible Faradaic electrolyte decomposition at the CC surface. For the G1 solvent, the amount of irreversible charge was relatively larger in the more cathodic potential range (0−0.3 V). A plot of the charge passed vs time for NaFSI in G1 is shown in Figure S11, which indicates that ∼0.002 mAh/cm^2 of the charge passed during the first CV cycle was irreversible. This first cycle irreversibility of NaFSI in G1 was calculated across three different cells, with the average value (35%) and standard deviation shown in blue in Figure 3c.

We next examined the CV cycling behavior of NaFSI in G2−G4 (with multiple cycles included in Figure S12). Figure 3b shows the first CV cycle of each electrolyte normalized and overlaid onto that of NaFSI in G1. The reductive sweeps matched well from 0.3 to 0 V for all NaFSI electrolytes. The reductive curve of NaFSI in G2 was broadly similar to that of G1 but with slightly more irreversible reduction at higher potentials. The first cycle irreversibility increased by 5% (red bar, Figure 3c) to 40% on average across three cells.

Interestingly, the reductive peaks near 0.9 V for both the G3 and G4 electrolytes corresponded with a large increase in first cycle irreversibility at 52 and 49%, respectively. To investigate whether any surface passivation that occurred at more cathodic potentials (0−0.3 V) impacted the reversibility of the 0.9 V reaction, we next performed CV for the NaFSI electrolytes between 0.4 and 2 V (Figure S13). The first cycle irreversibility of the 0.9 V reaction mirrored the trend of Figure 3c for all electrolytes, which confirms that the reduction reaction at this higher potential is largely irreversible. Together, these results indicate a connection between electrolyte formulation and irreversible capacity, and suggest that glyme length alters the relative proportions of decomposition products obtained from the 0.9 vs 0.3 V reactions.

The amount of irreversible charge associated with these pre-plating processes is consistent with the formation of an SEI layer with a thickness comparable to those reported in literature. While a detailed analysis of the composition of this "pre-plating SEI" will be presented in the following sections, for the sake of simplicity, we consider the formation of an inorganic NaF layer. This is a reasonable first-order approximation, as we have previously determined that salt species are prominent reactants at these pre-plating potentials, and NaF is the most commonly identified SEI component derived from fluorinated anions.[6,11] Under these simplifying assumptions, the irreversible charge capacity that is passed during the first CV cycle corresponds to SEI formation of a thickness of ∼12 nm (further details in the Supplementary Analysis section of the Supporting Information). Notably, this is the same order of magnitude of the postcycling SEI observed via both XPS sputtering (∼4 nm)[6] and cryogenic scanning transmission electron microscopy (∼25−30 nm)[11] of $NaPF_6$ in glymes. This further illustrates the importance of analyzing the formation of a pre-plating SEI in this study, which can dramatically alter the surface chemistry of the CC upon which Na nucleation and growth will occur.

We also note that there are two small features in the oxidative sweeps of all four electrolyte formulations. These features occurred near 0.7 and 1.3 V—approximately 0.4 V more positive than each of the reductive features near 0.3 and 0.9 V—which suggests some degree of reversibility for both of the associated reduction reactions. Prior work has shown that in addition to the reductive SEI components, the presence of surface oxides on the CC may also play a role in this redox behavior, which can participate in quasi-reversible conversion reactions with Na[29,64] or can chemically react with the alkali metal (as has been demonstrated with Li).[27] Aurbach et al. have also demonstrated that surface oxides can modulate the underpotential plating and stripping processes of Li metal, leading to both cathodic and anodic peaks at positive potentials vs Li/Li^+ on noble metal electrodes.[65] These redox processes may also correspond to the reversible (electro)-dissolution of Na-based SEI phases.[66,67] Nevertheless, what this electrochemical behavior suggests is that in addition to the electrolyte composition, which is our focus here, the CC surface chemistry plays a role in the pre-plating SEI. These pre-plating reactions are also of particular scientific interest for anode-free systems, as the electrochemical reversibility of SEI components is otherwise convoluted by the Faradaic current associated with plating and stripping phenomena, which may have their own sources of Coulombic inefficiency. Given the importance of surface chemistry to these various interfacial mechanisms, we next performed compositional analysis on the pre-plating SEI.

Compositional Analysis of the Pre-Plating SEI

Given the distinct electrochemical signatures observed above 0 V vs the Na electrode for the different electrolyte formulations during the previous section (Figures 1 and 2), we hypothesized that we would observe compositional differences on the CC surface with different glyme lengths. We continued to utilize the NaFSI formulations as a model system given the salt's solubility in all four glymes, with additional analyses of other relevant salts included in the Supporting Information. We performed constant current, constant voltage (CC/CV) measurements to systematically investigate pre-plating SEI compositions at a range of potentials: 1, 0.75, 0.5, 0.25, and 0 V. Further details on the experimental protocols, as well as representative voltage and current profiles for NaFSI in G1−G4, are shown for reference in Figure S14. Samples were cut in half after preparation, with one-half designated for ATR-FTIR and the other for XPS.

We first performed ATR-FTIR because of the technique's high surface sensitivity. It has been previously demonstrated by Aurbach et al. that the decomposition of Li-based electrolytes at pre-plating potentials can form infrared (IR)-active surface films, with the resulting IR spectra containing signatures of organic bonds similar to those seen in the bulk electrolyte, as well as the emergence of new species derived from solvent decomposition.[65,68] We reasoned that ATR-FTIR should likewise detect compositional changes in the nanoscale pre-plating SEI layer associated with solvent decomposition in Na electrolytes. Ether groups are IR-active, with C−O stretching vibrational modes observed near 1100 cm^{-1} for G1−G4 in the liquid state.[69] These vibrational modes have been reported to shift to near 1070 cm^{-1} when the ether oxygen is coordinated to Na^+ in the bulk liquid electrolyte.[13,16,70,71] We therefore focused on these wavenumber regions when analyzing the pre-plating SEI.

Figure 4 shows the IR spectra of the Al CC surface after CC/CV experiments using NaFSI in G1−G4. For each electrolyte formulation, a coin cell from the same batch was held at OCV over the course of the experiment, with the IR spectra of these Al CCs labeled "OCV" in gray. Given the rinsing and vacuum-drying process for each sample, as well as the nanoscale thickness of these surface films, it is unlikely that there are significant quantities of liquid electrolyte entrapped on the CC surface. We therefore interpret IR features in these wavenumber regions to correspond to solid glyme-derived species in the SEI that are formed upon electrolyte decomposition, the most probable of which are Na alkoxides.[65] Na methoxide (NaOMe) and Na ethoxide (NaOEt) reference samples, shown in Figure S15,[72,73] exhibited dominant IR peaks at 1061 and 1084 cm^{-1} for NaOMe and at 1110 cm^{-1} for NaOEt. Accordingly, we ascribe IR features from approximately 1050−1090 cm^{-1} to NaOMe, indicated by the red band in Figure 4, and features from approximately 1090−1125 cm^{-1} to correspond to either NaOEt or non-Na^+-coordinated C−O moieties[69] (as possible in longer-chain alkoxide species), indicated by the gray band in Figure 4.

For the pre-plating SEI of all NaFSI in glyme electrolytes (Figure 4a−d), Al CCs held at OCV exhibited weak transmittance features in both C−O stretching regions. This indicates a nonzero amount of C−O-containing species on the CC surface arising from chemical exposure to the electrolyte. A

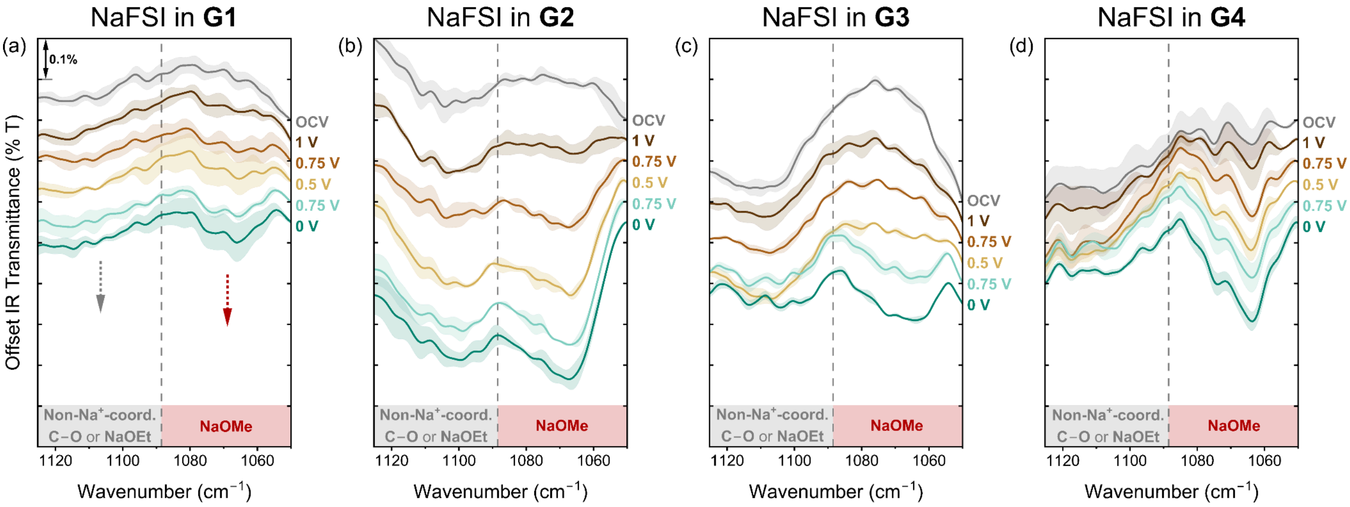

Figure 4. IR spectra of pre-plating SEI derived from NaFSI in glymes. (Top) Offset IR transmittance spectra for samples held at OCV, 1 V, 0.75, 0.5, 0.25, or 0 V for 2 h in NaFSI in (a) G1, (b) G2, (c) G3, or (d) G4. Peaks in the gray wavenumber region are assigned to non-Na^+-coordinated C−O stretching modes[69] or Na ethoxide species,[72] and peaks in the red region are assigned to Na methoxide species.[72] The vertical axis scaling is equal across all columns, with a scale bar of 0.1% transmittance (%T). Curves are vertically offset for comparison purposes. Each curve corresponds to the average of three spectra, with the surrounding shaded area corresponding to one standard deviation.

separate Al CC rinsed with G1 and then dried also showed similar features in these same regions (Figure S16). Together, these observations suggest that some degree of interfacial chemical reaction between the CC and the solvent occurs prior to the application of Faradaic current,[74] possibly driven by degradation pathways involving electrolyte impurities. As the applied potential decreased from 1 to 0 V, however, a clear emergence of IR features near 1070 cm^{-1} occurred, consistent with NaOMe formation. Difference spectra with respect to the OCV sample confirmed a monotonic increase in NaOMe with decreasing potential (Figures S17 and S18) for the pre-plating SEI of all electrolytes. In contrast, there were negligible changes in the amount of non-Na^+-coordinated C−O species or NaOEt within error (Figure S18).

We also note that there were changes in the relative shapes and intensities of IR features within the NaOMe region (most notably near 1058, 1066, 1073, and 1082 cm^{-1}). These distributions of features indicate subtle differences in the local electronic and bonding environments of alkoxide species across the different pre-plating SEI, which further suggests that solvent decomposition pathways are influenced by glyme length. Overall, these data support the presence of a pre-plating SEI—and notably, one that contains organic species even prior to Na deposition.

To investigate whether alkoxide species were present with the other electrolytes, we also examined the IR spectra of the pre-plating SEI from $NaPF_6$ in G1, G2, and G4 (Figure S19) and NaOTf in G1 and G3 (Figure S20) at these same applied potentials. These electrolyte formulations were chosen to compare the behavior of G1 vs longer-chain glymes (G2−G4) using the same salts as earlier. $NaBF_4$ was insoluble in G1 and thus excluded from further analysis. As the applied potential decreased from 1 to 0 V for all of these electrolytes, the pre-plating SEI similarly exhibited monotonic increases in NaOMe. This suggests broader similarities in solvent decomposition behavior when these salts are used, in accordance with the similar electrochemical features of Figure 2.

We also examined the IR spectra of NaTFSI in G1−G4. We previously showed in Figure S9 that these electrolytes exhibited different electrochemical behavior than the other fluorinated electrolytes. Figure S21 plots the IR spectra of the pre-plating SEI obtained through CC/CV for each NaTFSI electrolyte, with LSV included for reference. Notably, the amount of alkoxides in the pre-plating SEI of NaTFSI in G3 and NaTFSI in G4 increased from 1 to 0.5 V, but remained constant from 0.5 to 0 V. Interestingly, the changes in electrochemical behavior for these electrolytes correlated with changes in CC surface chemistry—and thus different physicochemical properties (e.g., electronic and ionic conductivity) of the pre-plating SEI, as further discussed in the Supplementary Analysis.

Because IR spectroscopy is limited to vibrational modes that induce a change in dipole moment, we next employed XPS as a complementary technique, using the other half of each pre-plating SEI sample. The pre-plating SEI of NaFSI in G1−G4 formed at the full range of applied potentials (1 V through 0 V) were again examined first. Elemental analysis based on the XPS survey scans (Figure S22) indicates that the spatially averaged surface compositions for all samples were majority O (40−48%), C (17−29%), and Al (20−25%), with minor Na (5−10%) and F (1−6%) components and trace amounts of S (≤2.6%) and N (≤1.6%). High-resolution core scans and component peak quantification for each sample are included in the Supporting Information (Figures S23−S30, with associated references and supplemental discussion). In contrast to the IR data, the XPS data showed no obvious trends in pre-plating SEI composition as a function of applied potential. This highlights the importance of utilizing complementary techniques to XPS that can identify more subtle changes associated with surface chemical bonding environments, in particular organic phases with unique vibrational fingerprints. Nevertheless, we observed distinct differences in the pre-plating SEI composition across the different electrolyte formulations.

The C 1s spectra of the pre-plating SEI formed at 0 V from different NaFSI-based formulations are shown in Figure 5a. The C 1s spectra exhibited at least four distinct peaks. We assigned the peak at ∼285 eV to C−C moieties (dark gray) and the peak at ∼286.5 eV (blue) to C−O moieties.[75] C−C

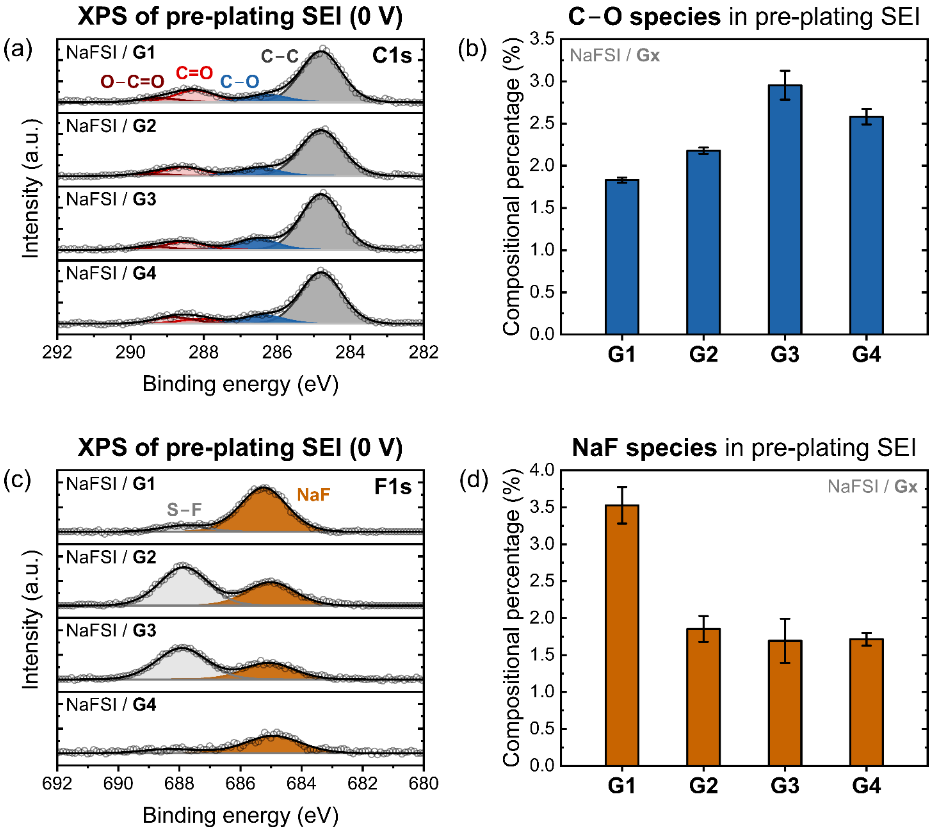

Figure 5. XPS of pre-plating SEI formed at 0 V for NaFSI in glymes. (a) C 1s spectra of the surface species from the NaFSI in G1−G4 samples. Spectra were calibrated to the adventitious (C−C) carbon at 284.8 eV.[75] C−O occurs at ∼286.5 eV.[75] The peaks at ∼288 and ∼289 eV were assigned to C═O and O−C═O moieties, respectively,[75] as discussed in the Supporting Information. (b) Compositional percentage of C−O species in the pre-plating SEI, calculated by applying C 1s peak deconvolution to the atomic percentages obtained via survey scan. (c) F 1s spectra from the NaFSI in G1−G4 samples. NaF occurs at ∼685 eV and S−F (from residual or fragmented NaFSI salt) at ∼688 eV.[6,75] (d) Relative amounts of NaF, calculated via F 1s peak deconvolution and atomic percentages. (b) and (d) display the average value for two detection spots per sample, with the error bars denoting the minimum and maximum values.

can be attributed mainly to adventitious carbon, with glyme-based decomposition products such as NaOEt also possible.[76] The C−O moieties are attributed mainly to Na alkoxides, with NaOMe the most likely species based on the previous IR data. Alkoxides are the most likely product following scission of one of the ether (C−O−C) bonds in a glyme molecule; both methoxide and ethoxide references are reported to contain a C−O component peak in XPS.[76] We assigned the peaks at ∼288 eV and ∼289 eV to carbonyl (C═O) and carboxyl (O−C═O) moieties, respectively, given their binding energies.[75] However, these species are not expected to form via the reduction of glyme-based electrolytes and may derive from various other solvent, salt, and/or contaminant species as discussed in the associated text of Figure S23.[12,17,75−78] While the rinsing, drying, and sample loading conditions were consistent among the different samples, systematic differences in the amount of adventitious carbon or other possible contaminants cannot be ruled out, so we focus our analysis on the C−O component peak.

The compositional percentage of C−O species in the pre-plating SEI of each electrolyte formulation is shown in Figure 5b. This percentage was calculated by weighting the atomic percentage of C obtained via survey scan by the deconvoluted peak areas from the C 1s spectra; additional calculation details are included in the Supporting Information. The bar plot represents the average value from two detection spots on the sample, with the error bars denoting the minimum and maximum values. We observed a general increase in alkoxide species moving from G1 to the longer-chain glymes G2−G4, with the largest quantity of alkoxides detected for the G3 formulation. Figure S31 shows the relative proportion of C−O in the pre-plating SEI formed at all applied potentials (1 V through 0 V); this general trend for the amount of alkoxides was consistent across the other samples.

Figure 5c shows the F 1s spectra of the pre-plating SEI formed at 0 V from the different NaFSI-based formulations. Two distinct peaks were observed: NaF at ∼685 eV and S−F species at ∼688 eV.[6,16,75,79] We attribute the majority of S−F species detected via XPS to residual or fragmented NaFSI salt ($NaN(SO_2F)_2$), given that the S−F peaks in the F 1s spectra corresponded to salt-based peaks[17,75,79,80] in the S 2p and N 1s spectra of the same samples (Figures S24−S26). Nevertheless, the presence of NaF indicates that decomposition of the FSI^- anion did occur. This is further supported by the fact that NaF peaks in the F 1s spectra corresponded to similar proportions of decomposed salt products (SO_x, Na_3N, or NSO^-)[6,17,75,79] in the S 2p and N 1s spectra, respectively. The relative proportions of NaF in the pre-plating SEI are shown in Figure 5d, with the other salt-derived products included in Figure S32. Notably, the proportion of NaF species in the G1-based formulation was nearly double those of the longer-chain glymes. In contrast to the nonmonotonic trend observed for the alkoxide species of Figure 5b, which peaked at G3, the amount of NaF species was roughly constant for G2−G4.

We also examined the pre-plating SEI of both NaFSI in G1 and NaFSI in G3 formed at a potential of 0 V using SEM-EDS, as shown in Figures S33−S35. These two electrolytes were chosen as representative for the short vs long chain glymes. Al dominated the EDS spectra for the two samples, and there were no discernible differences in their microscale morphology compared to a bare Al CC. This further supports that the thickness of the pre-plating SEI is at the nanoscale. Both the G1 and G3 samples exhibited spatially heterogeneous distributions of F-containing species at the microscale via EDS, which indicates the presence of salt-decomposition products and/or residual salt, both of which are consistent with the XPS data. Notably, there was a considerably more homogeneous distribution of both the Na and C signal in the G3 sample, which suggests a relatively uniform coverage of Na alkoxide species at the microscale with sufficient thickness for EDS detection. Future experiments to probe physicochemical heterogeneity at the nanoscale using techniques such as cryogenic transmission electron microscopy[81,82] will be useful to analyze the impact of the pre-plating SEI on ensuing Na nucleation and growth.

The presence of organic alkoxide species on the CC surface with applied potential suggests that the pre-plating reactions of Figure 2 facilitate solvent decomposition, either directly (via electrochemical reduction of a glyme at the interface) or indirectly (via chemical reaction between a glyme and another reduced product in the electrolyte). While the electrochemical data suggests the latter, this warranted further investigation into the formation mechanisms of the pre-plating SEI. Furthermore, the different proportions of salt vs solvent decomposition products observed herein (Figure 5) provide evidence that the interphase composition is influenced by electrolyte formulation—in particular glyme length. As the four glymes are chemically similar, we hypothesized that these changes in pre-plating SEI composition must result from mechanistic changes of electrolyte decomposition caused by changes in the Na^+ coordination environment. We therefore next examined Na^+ speciation in these electrolytes.

Impact of Na^+ Coordination in the Electrolyte on Pre-Plating SEI Composition

We first examined the distribution of Na^+−anion coordination environments within the bulk electrolytes NaFSI in G1−G4 using Raman spectroscopy. Figure 6a shows the Raman spectra of NaFSI in G1 (top) through G4 (bottom). Raman features in this wavenumber range are associated with expansion/contraction vibrational modes of the FSI^- anion, which are especially sensitive to cation coordination.[83] Spectra are normalized to the total area of the component peaks, as the salt concentration was constant among the four electrolytes, but the background fluorescence varied between samples. The blue component peak near 718 cm^{-1} is attributed to FSI^- anions that are either not coordinated to Na^+ ("free") or in a solvent-separated ion pair (SSIP) with Na^+.[17,79,83] The orange peak near 729 cm^{-1} is attributed to FSI^- in a contact ion pair (CIP) with Na^+, and the red peak near 740 cm^{-1} is attributed to FSI^- in an aggregate (AGG) configuration.[17,79,83] Peak fitting parameters are shown in Table S1. Based on these fits, the broad distribution of FSI^- anions in the bulk electrolyte for each glyme is shown in Figure 6b, which agrees with the predicted distribution by classical molecular dynamics (MD) simulations shown in Figure S36.[84]

Free/SSIP FSI^- anions represented the largest relative fraction for all glymes, but the amount of free/SSIP FSI^- did increase considerably from G1 (56%) to G3 (80%) then slightly decreased for G4 (72%). In other words, electrolytes with longer glymes exhibited lesser degrees of Na^+−FSI^- coordination, and thus greater degrees of Na^+−glyme coordination. Notably, this trend mirrors that of the alkoxide species in the pre-plating SEI of NaFSI in G1−G4 shown during XPS (previously shown in Figure 5b). This trend indicates that an increase of solvent-derived products within the pre-plating SEI correlated with an increase of Na^+−glyme coordination in the bulk electrolyte. Furthermore, the amount of salt-derived NaF in each formulation (from Figure 5d) roughly followed the proportion of CIP, such that an increase in salt-derived products occurred with higher degrees of Na^+−FSI^- coordination. While a more detailed accounting of specific Na^+ coordination environments would benefit from future computational studies, these results suggest a broader connection between Na^+ coordination and the composition of the pre-plating SEI. We therefore extended this analysis to other Na-based electrolytes.

The Raman spectra and average distribution of OTf^- anions in the bulk electrolyte for NaOTf in G1−G4 are shown in Figure 6c,d. The OTf^- $\delta_s(CF_3)$ vibrational mode was utilized for fitting,[85] as peaks from the $\nu_s(SO_3)$ vibrational mode near 1030 cm^{-1} overlapped with glyme peaks in the Raman spectra. OTf^- was also observed to exist in free/SSIP, CIP, and AGG configurations.[85,86] NaOTf exhibited the same general speciation trends as NaFSI with respect to glyme length, but ion-pairing interactions were substantially more favorable in the NaOTf-based electrolytes. For example, NaOTf in G1 had majority AGG and minority CIP species, while NaOTf in G3 had majority CIP and minority free/SSIP species (and still the largest proportion of free/SSIP anions of the NaOTf series). Figure 6e,f show the Raman spectra and average anion distribution for NaTFSI in G1−G4. $TFSI^-$ expansion/contraction vibrational modes were used for fitting, with free/SSIP and CIP $TFSI^-$ observed.[87] NaTFSI again exhibited the same general speciation trends as NaFSI, with the least and most free/SSIP $TFSI^-$ observed for G1 and G3, respectively.

Given the largest differences in Na^+ speciation between the G1- and G3-based electrolytes, we next compared the pre-plating SEI derived from these specific electrolytes. Figure 6g shows the compositional percentages of solvent-derived (C−O) vs salt-derived (NaF) species in the pre-plating SEI formed at 0 V. The XPS spectra for NaFSI in G1 and G3 were shown previously in Figure 5, and the spectra for the NaOTf and NaTFSI electrolytes are shown in Figures S37 and S38.[6,14,75] Changes in PF_6^- coordination are not observable through conventional Raman vibrational modes[88] such that we could not obtain comparable $NaPF_6$ speciation data. Nevertheless, we also performed XPS on the pre-plating SEI of $NaPF_6$ in G1, G2, and G4 (Figures S39 and S40)[6,11,75] for the sake of comparison. Consistent with NaFSI, the pre-plating SEI of NaOTf, NaTFSI, and $NaPF_6$ all exhibited increases in C−O alkoxide content with the longer glymes (Figure 6g), providing further evidence that increased solvent decomposition correlates with an increase in Na^+−glyme coordination.

The salt-derived NaF content, on the other hand, exhibited surprising differences in behavior in Figure 6g. Unlike NaFSI, the pre-plating SEI of NaOTf exhibited slight increases in NaF content from G1 to G3. Interestingly, the NaF content in the pre-plating SEI of both NaFSI and NaOTf correlated with the

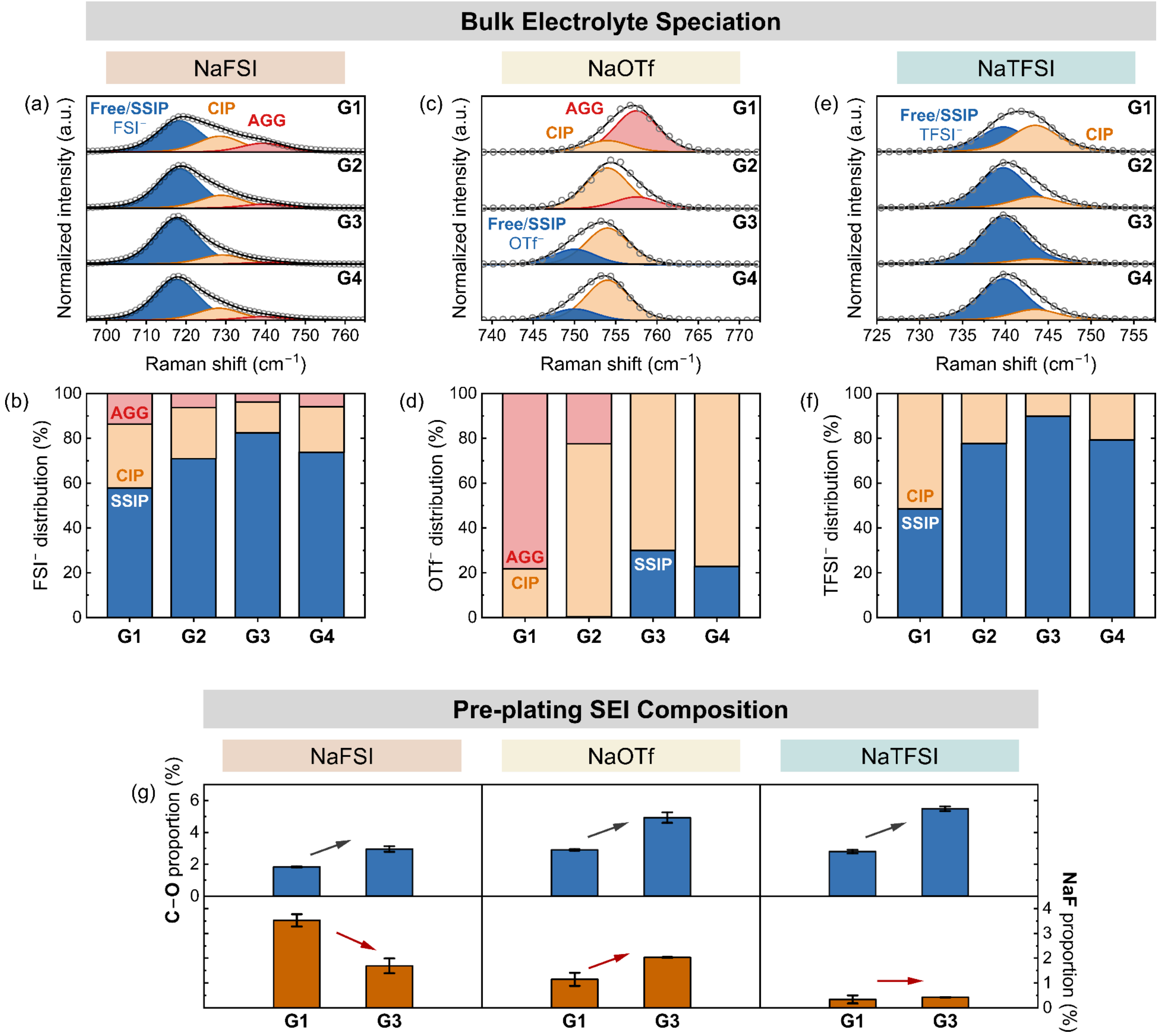

Figure 6. Relationships between bulk electrolyte speciation and pre-plating SEI composition in glyme-based electrolytes. (a) Raman spectra of NaFSI in G1–G4. The peak near 718 cm^{-1} is attributed to FSI$^-$ anions that are either uncoordinated to Na$^+$ (free) or in a solvent-separated ion pair (SSIP) with Na$^+$, the peak near 729 cm^{-1} is attributed FSI$^-$ in a contact ion pair (CIP) with Na$^+$, and the peak near 740 cm^{-1} is attributed to FSI$^-$ in an aggregate (AGG) configuration.[17,83] (b) The average distribution of FSI$^-$ anions in each glyme in the bulk electrolyte, based on the Raman spectra. (c) Raman spectra and (d) the average distribution of OTf$^-$ anions for NaOTf in G1–G4. 750 cm^{-1} corresponds to free/SSIP OTf$^-$, 754 cm^{-1} corresponds to CIP OTf$^-$, and 758 cm^{-1} corresponds to AGG OTf$^-$.[85,86] (e) Raman spectra and (f) the average distribution of TFSI$^-$ anions for NaTFSI in G1–G4. 740 cm^{-1} corresponds to free/SSIP TFSI$^-$, and 744 cm^{-1} corresponds to CIP TFSI$^-$.[87] All spectra are normalized to the total area of the component peaks. (g) Pre-plating SEI components from NaFSI, NaOTf, and NaTFSI in G1 or G3, formed at a potential of 0 V for 2 h, based on the XPS spectra of Figures 5 and S37 and S38. The compositional percentage of C–O and NaF species in the pre-plating SEI are shown, calculated from atomic percentages from the survey scans and deconvoluted peak areas from the C 1s and F 1s scans, respectively. The average value for two detection spots per sample is displayed, with the error bars denoting the minimum and maximum values.

amount of CIP (not AGG) in their respective bulk electrolytes. This correlation suggests that Na$^+$–anion coordination facilitates anion decomposition at the interface at pre-plating potentials (to form NaF among other species, see Supplementary Analysis),[89−98] with the assumption that CIP reduction is more likely to occur than AGG reduction due to transport and/or kinetic limitations. On the other hand, the amount of NaF in the pre-plating SEI of NaTFSI was comparatively low, and roughly constant for both G1 and G3. However, the proportion of CF_3/RCF_x-containing phases (Figure S38) was significantly larger than NaF and did correlate with CIP TFSI$^-$ in the bulk electrolyte. This suggests that TFSI$^-$ decomposition primarily occurs via the scission of the S–C bond in these electrolytes instead of direct fluoride abstraction (Supplementary Analysis).[98−100] While direct analysis of anion decomposition mechanisms requires further investigation, we interpret the data of Figure 6 to indicate that Na$^+$–anion coordination also modulates the pre-plating SEI composition, with a mechanism-dependent impact on the proportions of salt-derived phases.

Given the correlation between Na$^+$ coordination and electrolyte-derived species in the pre-plating SEI—in particular the trends in C–O species observed for all Na electrolytes examined herein—we further examined the link between Na$^+$ coordination and solvent decomposition. This was also motivated by the reported thermodynamic and electrochemical

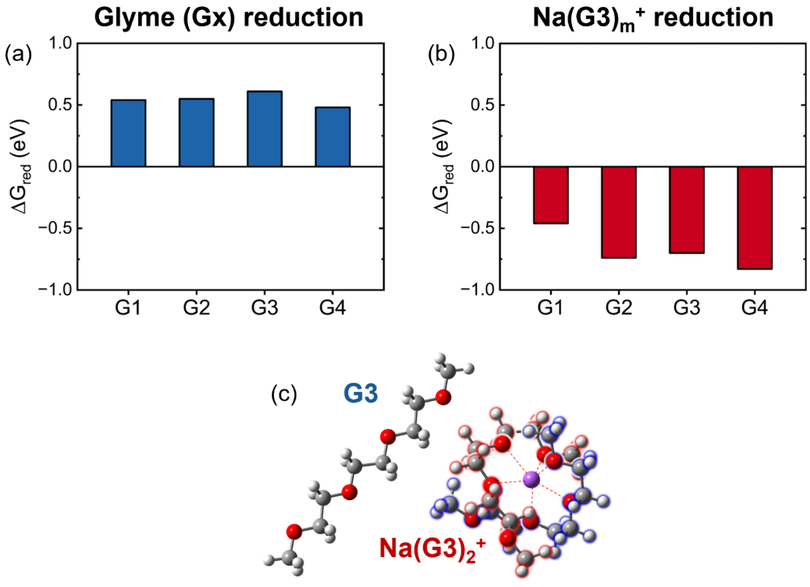

Figure 7. Thermodynamics of G1−G4 reduction from DFT calculations. Gibbs free energy of one-electron reduction of an (a) uncoordinated glyme molecule vs (b) multiple glyme molecules coordinated with Na^+ ($Na(Gx)_m^+$, m = 2 or 3) with a fixed Na−O coordinated of 6, as detailed in the Supporting Information. (c) Representative geometries for an uncoordinated G3 vs $Na(G3)_2^+$.

stability of glymes.[19,20] It has been reported that Li^+ coordination environments can alter the redox potential of Li plating/stripping (0 V vs Li/Li^+),[61,101] which in turn alters the thermodynamic driving forces of electrolyte decomposition and ensuing SEI formation onto the surface of plated Li metal.[101] We thus examined whether shifts in the redox potential of Na/Na^+ may also impact SEI formation at more positive (pre-plating) potentials. We measured relatively minor shifts in the redox potential of the Na electrode (~0.1 V) with increasing glyme length (as discussed in Figure S41),[61,102,103] which we do not anticipate to be a dominant factor in determining the reaction pathways and product formation at pre-plating potentials.

We next used computational modeling to study the influence of the solvation environment on the thermodynamics of glyme decomposition. We began by examining the decomposition reaction free energies of neat glyme molecules, G1−G4. The dissociation reaction was modeled as C−O bond cleavage (Reaction R1) to yield a methoxy fragment (OCH_3) and the complementary fragment, as Seguin et al. discussed:[104]

$$CH_3(OCH_2CH_2)_nOCH_3 \rightarrow CH_3(OCH_2CH_2)_n + OCH_3 \qquad \text{(R1)}$$

where n = 1 to 4 for G1−G4, respectively. The DFT-computed decomposition reaction free energies (ΔG_{decomp} in eV) for neutral and anionic (one-electron reduced) glymes are shown in Table S2. The free energies of the one-electron reduction of neat neutral glyme molecules are also included.

For neutral glyme molecules, the decomposition free energy is consistently high and endergonic (≥2.85 eV), as expected. However, upon electrochemical reduction of glyme, decomposition from the reduced glyme species to an OCH_3^- anion species and a radical is exergonic in the range of $\Delta G_{decomp.}$ = −1.59 to −1.69 eV. Note that several cleavage schemes were considered depending on electron distribution during bond dissociation (e.g., homolytic vs heterolytic cleavage), and the lowest-energy reactions were selected for analysis (Figure S42). These computational results indicate that electrochemical reduction of glymes is required for decomposition reaction, since neutral molecules are thermodynamically stable vs Na. However, the consistently endergonic free energy of reduction shown in Figure 7a (0.48−0.61 eV) shows that the direct electrochemical reduction of bare glymes is thermodynamically unfavorable (highly negative onset potentials; further details are included in the Supplementary Analysis section of the Supporting Information).

Guided by these findings, we further studied the decomposition of glymes coordinated to a Na^+ cation. Only reduced Na^+−glyme species (with a net zero charge) were considered for decomposition given the increased reactivity discussed above. We first examined the possible decomposition pathways of a single glyme molecule (G1−G4) coordinated to Na^+, as shown in Figure S43, to better discern the reaction tendencies using a simple system. Reaction R2 (below) is the most energetically favorable decomposition pathway of the prereduced Na^+−glyme clusters after reduction, exhibiting exergonic free energies ($\Delta G_{decomp.}$ = −0.63 to −0.95 eV) for all four Na^+-coordinated glyme species after reduction.

$$\begin{aligned} &Na - CH_3(OCH_2CH_2)_nOCH_3 \\ &\quad \rightarrow CH_3(OCH_2CH_2)_n + Na - OCH_3 \qquad \text{(R2)} \end{aligned}$$

The decomposition products for this reaction are neutral Na methoxide and the complementary radical fragment; this is consistent with the presence of Na methoxide detected herein by IR spectroscopy (Figure 4). The geometries and reduction free energies of these single-glyme coordinated species ($(Na(Gx)_1^+)$) are shown in Figure S44. Compared with neat glymes, the reduction free energies are more exergonic by −1.1 to −1.8 eV, indicating a greater propensity for reduction and thus decomposition when the glyme molecules are coordinated with Na.

Since the ion coordination environment strongly influences reactivity prediction in DFT,[105,106] we next performed free energy calculations of Na^+−glyme clusters that contained multiple glyme molecules with the Na^+ coordination number held constant at six: three G1 molecules (with bidentate coordination) or two G2−G4 molecules (with tridentate coordination), as shown in Figure S45. The corresponding decomposition reaction scheme is shown in Reaction R2a for reduced clusters (net zero charge):

$$\mathrm{Na} - [\mathrm{CH_3(OCH_2CH_2)_nOCH_3}]_m$$

$$\rightarrow \mathrm{CH_3(OCH_2CH_2)}_n + (\mathrm{Na} - \mathrm{OCH_3})[\mathrm{CH_3(OCH_2CH_2)_n} \mathrm{OCH_3}]_{m-1} \tag{R2a}$$

where m = number of glyme molecules (2 or 3), and n = 1 to 4 for G1 to G4, respectively. The free energy of one-electron reduction of these multiple-glyme coordinated species ($\mathrm{Na(Gx)}_m^+$) is shown in Figure 7b. In this case, the reduction was considerably less exergonic for the G1-based coordination environments (−0.46 eV) compared to those of the longer-chain glymes (−0.70 to −0.83 eV), representing a clear demarcation in reduction behavior between G1 and G2−G4 when glymes are the sole solvating species, which is in good agreement with the experimental trends observed in Figure 6.

Overall, these DFT calculations demonstrate that $\mathrm{Na^+}$ coordination markedly increases the thermodynamic driving force for glyme breakdown via reduction-triggered decomposition. Furthermore, the multimolecule cluster model reproduces the instability of longer glymes, which agrees with the experimentally observed irreversibility. It is important to note that the magnitude of the reduction free energies of the clusters remains at a moderate level, which corresponds to negative potentials vs $\mathrm{Na/Na^+}$ in this particular computational model (details in the Supplementary Analysis section). However, experimentally we observe that glyme-derived SEI species are present at pre-plating potentials (>0 V). Therefore, additional factors need to be considered to fully describe the pre-plating SEI formation behavior. While a detailed computational study of these factors is beyond the scope of this paper, we outline several possible contributions[65,93,107−110] in the Supplementary Analysis.

■ CONCLUSION

In this work, we have systematically examined the formation and composition of the pre-plating SEI that forms on Al current collectors in a range of glyme-based Na electrolytes. By correlating electrochemical reduction events and ex situ compositional analysis, we demonstrate that electrolyte decomposition can occur at potentials significantly more positive than the onset of Na plating, forming both solvent- and salt-derived SEI products. The amount of organic alkoxide phases in the pre-plating SEI can be predictably modulated by glyme chain length, in agreement with $\mathrm{Na^+}$ coordination trends in the bulk electrolyte. The amount of salt-derived components also correlates with $\mathrm{Na^+}$−anion coordination, though the specific phases present are dependent on the anion. While prior work on studying the SEI in Na electrolytes has primarily focused on the reactions that occur on the surface of the plated (metallic) Na phase, the insights from this study help us to build a more complete understanding of the relationships between electrolyte composition, SEI formation, and the surface chemistry of the CC.

While the overall loss of Na inventory in a battery associated with this nanoscale pre-plating SEI formation is small, we hypothesize that the implications of its presence on the subsequent cycling processes of a Na metal anode are significant. For example, while the CC in anode-free systems is often idealized as a single metallic phase, the chemical composition (and associated heterogeneity) of the surface is known to play a critical role in the nucleation and growth behavior of the subsequent plating and stripping process.[24] As we show here, the formation of a composite pre-plating SEI layer can be systematically tuned by controlling both electrolyte formulation and applied potential—analogous to a battery formation cycle.[28] The resulting composition and phase of the surface layer will dramatically alter key functional properties including electronic and ionic conductivity (impacting overpotential and transport processes), surface energy (impacting wetting and critical radius for nucleation), and current focusing along the surface. These material properties will, in turn, alter the nucleation process on the CC and affect critical figures of merit, including Coulombic efficiency and stability.[111] Additionally, the presence of surface passivation layers on the CC also controls galvanic corrosion processes in anode-free systems, which will influence the calendar life of the battery.[28,112]

While the focus of the present study was on developing a fundamental understanding of the relationships between electrolyte formulation and the surface chemistry of the resulting pre-plating SEI, future work can expand upon this knowledge to explore the ability to leverage these "tuning knobs" to alter the CC surface with the goal of rationally controlling the subsequent plating and stripping processes. The detailed chemical analysis of the pre-plating SEI composition reported herein can also be used to inform computational models that better describe the early stages of nucleation on the CC surface, with respect to key parameters that will influence the electrochemical reduction of $\mathrm{Na^+}$ ions to neutral adatoms, the surface diffusion and coalescence of Na into critical nuclei, and the crystallization and growth of Na deposits.[24] Ultimately, this study shows how these material properties all link back to the electrolyte composition, providing insights into rational design of next-generation electrolytes from a molecular perspective.

■ ASSOCIATED CONTENT

Supporting Information

The Supporting Information is available free of charge at https://pubs.acs.org/doi/10.1021/jacsau.6c00193.

> Experimental and computational methods; supplemental electrochemical analysis; Fourier-transform infrared spectroscopy; X-ray photoelectron spectroscopy; scanning electron microscopy and energy dispersive X-ray spectroscopy; molecular dynamics; density functional theory; and supplementary analysis and discussion (PDF)

■ AUTHOR INFORMATION

Corresponding Author

Neil P. Dasgupta − *Department of Mechanical Engineering and Department of Materials Science and Engineering, University of Michigan, Ann Arbor, Michigan 48109, United States; Energy Storage Research Alliance, Argonne National Laboratory, Lemont, Illinois 60439, United States;* orcid.org/0000-0002-5180-4063; Email: ndasgupt@umich.edu

Authors

Aaron M. Melemed − *Department of Mechanical Engineering, University of Michigan, Ann Arbor, Michigan 48109, United States; Energy Storage Research Alliance, Argonne National Laboratory, Lemont, Illinois 60439, United States*

Sungil Hong − *Materials Science Division, Argonne National Laboratory, Lemont, Illinois 60439, United States; Energy Storage Research Alliance, Argonne National Laboratory, Lemont, Illinois 60439, United States;* orcid.org/0000-0001-8729-0861

Jonathan R. Thurston − *Department of Mechanical Engineering, University of Michigan, Ann Arbor, Michigan 48109, United States; Energy Storage Research Alliance, Argonne National Laboratory, Lemont, Illinois 60439, United States*

Alexis Luglio − *Department of Materials Science and Engineering, University of Michigan, Ann Arbor, Michigan 48109, United States; Energy Storage Research Alliance, Argonne National Laboratory, Lemont, Illinois 60439, United States*

Ethan B. Rose − *Department of Mechanical Engineering, University of Michigan, Ann Arbor, Michigan 48109, United States; Energy Storage Research Alliance, Argonne National Laboratory, Lemont, Illinois 60439, United States*

Thomas S. Marchese − *Pritzker School of Molecular Engineering, University of Chicago, Chicago, Illinois 60637, United States; Energy Storage Research Alliance, Argonne National Laboratory, Lemont, Illinois 60439, United States*

Jianwei Lai − *Chemical Sciences Division and Advanced Light Source, Lawrence Berkeley National Laboratory, Berkeley, California 94720, United States; Energy Storage Research Alliance, Argonne National Laboratory, Lemont, Illinois 60439, United States;* orcid.org/0000-0001-5841-1134

Ethan J. Crumlin − *Chemical Sciences Division and Advanced Light Source, Lawrence Berkeley National Laboratory, Berkeley, California 94720, United States; Energy Storage Research Alliance, Argonne National Laboratory, Lemont, Illinois 60439, United States;* orcid.org/0000-0003-3132-190X

Ying Shirley Meng − *Pritzker School of Molecular Engineering, University of Chicago, Chicago, Illinois 60637, United States; Energy Storage Research Alliance, Argonne National Laboratory, Lemont, Illinois 60439, United States;* orcid.org/0000-0001-8936-8845

Nirala Singh − *Department of Chemical Engineering, University of Michigan, Ann Arbor, Michigan 48109, United States; Energy Storage Research Alliance, Argonne National Laboratory, Lemont, Illinois 60439, United States;* orcid.org/0000-0003-0389-3927

Rajeev S. Assary − *Materials Science Division, Argonne National Laboratory, Lemont, Illinois 60439, United States; Energy Storage Research Alliance, Argonne National Laboratory, Lemont, Illinois 60439, United States;* orcid.org/0000-0002-9571-3307

Complete contact information is available at: https://pubs.acs.org/10.1021/jacsau.6c00193

Notes

The authors declare no competing financial interest.

ACKNOWLEDGMENTS

This work is supported by the Energy Storage Research Alliance "ESRA" (DE-AC02-06CH11357), an Energy Innovation Hub funded by the U.S. Department of Energy (DOE), Office of Science, Basic Energy Sciences (BES). A. L. acknowledges support from the National Science Foundation Graduate Research Fellowship Program under Grant No. DGE-1256260. The authors acknowledge the Michigan Center for Materials Characterization for use of the instruments and staff assistance. S.H. and R.S.A. acknowledge computational supports from the Center for Nanoscale Materials, a U.S. Department of Energy Office of Science User Facility, supported by the U.S. DOE, Office of Basic Energy Sciences, under Contract No. DE-AC02-06CH11357 (User proposal No. 83823), and Bebop, a high-performance computing cluster operated by the Laboratory Computing Resource Center at Argonne National Laboratory. SEM analysis was performed on the Helios Hydra 5 PFIB-SEM at the Center for Nanoscale Materials, a U.S. Department of Energy Office of Science User Facility, was supported by the U.S. DOE, Office of Basic Energy Sciences, under Contract No. DE-AC02-06CH11357 under proposal 83856.

REFERENCES

(1) Hirsh, H. S.; Li, Y.; Tan, D. H. S.; Zhang, M.; Zhao, E.; Meng, Y. S. Sodium-ion batteries paving the way for grid energy storage. *Adv. Energy Mater.* **2020**, *10* (32), No. 2001274.

(2) Yang, T.; Luo, D.; Liu, Y.; Yu, A.; Chen, Z. Anode-free sodium metal batteries as rising stars for lithium-ion alternatives. *iScience* **2023**, *26* (3), No. 105982.

(3) Chen, Y.; Ye, C.; Zhang, N.; Liu, J.; Li, H.; Davey, K.; Qiao, S.-Z. Prospects for practical anode-free sodium batteries. *Mater. Today* **2024**, 73, 260−274.

(4) Zhao, Y.; Adair, K. R.; Sun, X. Recent developments and insights into the understanding of Na metal anodes for Na-metal batteries. *Energy Environ. Sci.* **2018**, *11* (10), 2673−2695.

(5) Lee, B.; Paek, E.; Mitlin, D.; Lee, S. W. Sodium metal anodes: emerging solutions to dendrite growth. *Chem. Rev.* **2019**, *119* (8), 5416−5460.

(6) Seh, Z. W.; Sun, J.; Sun, Y.; Cui, Y. A highly reversible room-temperature sodium metal anode. *ACS Central Science* **2015**, *1* (8), 449−455.

(7) Hobold, G. M.; Lopez, J.; Guo, R.; Minafra, N.; Banerjee, A.; Shirley Meng, Y.; Shao-Horn, Y.; Gallant, B. M. Moving beyond 99.9% Coulombic efficiency for lithium anodes in liquid electrolytes. *Nature Energy* **2021**, *6* (10), 951−960.

(8) Chen, K.-H.; Wood, K. N.; Kazyak, E.; LePage, W. S.; Davis, A. L.; Sanchez, A. J.; Dasgupta, N. P. Dead lithium: mass transport effects on voltage, capacity, and failure of lithium metal anodes. *Journal of Materials Chemistry A* **2017**, *5* (23), 11671−11681.

(9) Fang, C.; Li, J.; Zhang, M.; Zhang, Y.; Yang, F.; Lee, J. Z.; Lee, M.-H.; Alvarado, J.; Schroeder, M. A.; Yang, Y.; et al. Quantifying inactive lithium in lithium metal batteries. *Nature* **2019**, *572* (7770), 511−515.

(10) Hobold, G. M.; Gallant, B. M. Quantifying capacity loss mechanisms of Li metal anodes beyond inactive Li0. *ACS Energy Letters* **2022**, *7* (10), 3458−3466.

(11) Sayahpour, B.; Li, W.; Bai, S.; Lu, B.; Han, B.; Chen, Y.-T.; Deysher, G.; Parab, S.; Ridley, P.; Raghavendran, G. Quantitative analysis of sodium metal deposition and interphase in Na metal batteries. *Energy Environ. Sci.* **2024**, *17* (3), 1216−1228.

(12) Wang, S.; Chen, Y.; Jie, Y.; Lang, S.; Song, J.; Lei, Z.; Wang, S.; Ren, X.; Wang, D.; Li, X. Stable sodium metal batteries via manipulation of electrolyte solvation structure. *Small Methods* **2020**, *4* (5), No. 1900856.

(13) Goktas, M.; Bolli, C.; Buchheim, J.; Berg, E. J.; Novák, P.; Bonilla, F.; Rojo, T.; Komaba, S.; Kubota, K.; Adelhelm, P. Stable and unstable iglyme-based electrolytes for batteries with sodium or graphite as electrode. *ACS Appl. Mater. Interfaces* **2019**, *11* (36), 32844−32855.

(14) Cao, R.; Mishra, K.; Li, X.; Qian, J.; Engelhard, M. H.; Bowden, M. E.; Han, K. S.; Mueller, K. T.; Henderson, W. A.; Zhang, J.-G. Enabling room temperature sodium metal batteries. *Nano Energy* **2016**, *30*, 825−830.

(15) Schafzahl, L.; Hanzu, I.; Wilkening, M.; Freunberger, S. A. An electrolyte for reversible cycling of sodium metal and intercalation compounds. *ChemSusChem* **2017**, *10* (2), 401−408.

(16) Lee, J.; Lee, Y.; Lee, J.; Lee, S.-M.; Choi, J.-H.; Kim, H.; Kwon, M.-S.; Kang, K.; Lee, K. T.; Choi, N.-S. Ultraconcentrated sodium bis (fluorosulfonyl) imide-based electrolytes for high-performance sodium metal batteries. *ACS Appl. Mater. Interfaces* **2017**, *9* (4), 3723−3732.

(17) Zheng, J.; Chen, S.; Zhao, W.; Song, J.; Engelhard, M. H.; Zhang, J.-G. Extremely stable sodium metal batteries enabled by localized high-concentration electrolytes. *ACS Energy Letters* **2018**, *3* (2), 315−321.

(18) Doi, K.; Yamada, Y.; Okoshi, M.; Ono, J.; Chou, C. P.; Nakai, H.; Yamada, A. Reversible sodium metal electrodes: Is fluorine an essential interphasial component? *Angew. Chem.* **2019**, *131* (24), 8108−8112.

(19) Choquette, Y.; Brisard, G.; Parent, M.; Brouillette, D.; Perron, G.; Desnoyers, J. E.; Armand, M.; Gravel, D.; Slougui, N. Sulfamides and glymes as aprotic solvents for lithium batteries. *J. Electrochem. Soc.* **1998**, *145* (10), 3500.

(20) Tang, S.; Zhao, H. Glymes as versatile solvents for chemical reactions and processes: from the laboratory to industry. *RSC Adv.* **2014**, *4* (22), 11251−11287.

(21) Ren, X.; Wu, Y.; Chen, X.; Hu, L.; Zhao, Y.; Zhang, T.; Ge, B.; Sun, X.; Yu, X. Formulating ether-based electrolytes for highly reversible sodium metal anodes at high temperatures. *Energy Mater. Adv.* **2025**, *6*, 0184.

(22) Zhao, S.; Yu, Q.; Yang, S.; Wan, S.; Chen, J.; Xu, H.; Lou, X.; Chen, S. Constructing robust interphase via anion-enhanced solvation structure for high-voltage fast charging sodium metal batteries. *Nano Energy* **2025**, *138*, No. 110913.

(23) Shen, Y.; Xu, J.; Li, Y.; Che, H.; Zhao, S.; Ishaq, M.; Jabeen, M.; Zhang, Y.; Wu, J.; Li, J.; et al. Anion−cation synergistic interactions for low-temperature and fast-charging performance in sodium batteries. *J. Mater. Chem. A* **2025**, *13* (25), 19631−19643.

(24) Sanchez, A. J.; Dasgupta, N. P. Lithium metal anodes: Advancing our mechanistic understanding of cycling phenomena in liquid and solid electrolytes. *J. Am. Chem. Soc.* **2024**, *146* (7), 4282−4300.

(25) Chen, K.-H.; Sanchez, A. J.; Kazyak, E.; Davis, A. L.; Dasgupta, N. P. Synergistic effect of 3D current ollectors and ALD surface modification for high Coulombic efficiency lithium metal anodes. *Adv. Energy Mater.* **2019**, *9* (4), No. 1802534.

(26) Oyakhire, S. T.; Zhang, W.; Shin, A.; Xu, R.; Boyle, D. T.; Yu, Z.; Ye, Y.; Yang, Y.; Raiford, J. A.; Huang, W.; et al. Electrical resistance of the current collector controls lithium morphology. *Nat. Commun.* **2022**, *13* (1), 3986.

(27) Yoon, J. S.; Liao, D. W.; Greene, S. M.; Cho, T. H.; Dasgupta, N. P.; Siegel, D. J. Thermodynamics, adhesion, and wetting at Li/Cu(-oxide) interfaces: Relevance for anode-free lithium−metal batteries. *ACS Appl. Mater. Interfaces* **2024**, *16* (15), 18790−18799.

(28) Oyakhire, S. T.; Zhang, W.; Yu, Z.; Holmes, S. E.; Sayavong, P.; Kim, S. C.; Boyle, D. T.; Kim, M. S.; Zhang, Z.; Cui, Y.; et al. Correlating the formation protocols of solid electrolyte interphases with practical performance metrics in lithium metal batteries. *ACS Energy Letters* **2023**, *8* (1), 869−877.

(29) Karcher, F.; Uhl, M.; Geng, T.; Jacob, T.; Schuster, R. Entropic contributions to sodium solvation and solvent stabilization upon electrochemical sodium deposition from diglyme and propylene carbonate electrolytes. *Angew. Chem., Int. Ed.* **2023**, *62* (22), No. e202301253.

(30) Wang, L.; Zhang, K.; Hu, Z.; Duan, W.; Cheng, F.; Chen, J. Porous CuO nanowires as the anode of rechargeable Na-ion batteries. *Nano Research* **2014**, *7* (2), 199−208.

(31) Dettmann, L.; Colbin, L. O. S.; Naylor, A. J. Influence of battery electrode chemistry on electrolyte decomposition. *Advanced Materials Interfaces* **2025**, No. 2500262.

(32) Vaalma, C.; Buchholz, D.; Weil, M.; Passerini, S. A cost and resource analysis of sodium-ion batteries. *Nat. Rev. Mater.* **2018**, *3* (4), 18013.

(33) Quartarone, E.; Eisenmann, T.; Kuenzel, M.; Tealdi, C.; Marrani, A. G.; Brutti, S.; Callegari, D.; Passerini, S. Towards advanced sodium-ion batteries: Green, low-Cost and high-capacity anode compartment encompassing phosphorus/carbon nanocomposite as the active material and aluminum as the current collector. *J. Electrochem. Soc.* **2020**, *167* (8), No. 080509.

(34) Tang, F.; Xia, R.; Chen, D.; Yao, Y.; Liu, L.; Feng, Y.; Rui, X.; Yu, Y. Rapid and reversible Na deposition onto Al nanosheet arrays. *Journal of Energy Chemistry* **2022**, *74*, 1−7.

(35) *Gaussian 16, Revision C.01*; Gaussian, Inc.: Wallingford CT, 2016.

(36) Chai, J.-D.; Head-Gordon, M. Long-range corrected hybrid density functionals with damped atom−atom dispersion corrections. *Phys. Chem. Chem. Phys.* **2008**, *10* (44), 6615−6620.

(37) Rassolov, V. A.; Pople, J. A.; Ratner, M. A.; Windus, T. L. 6−31G* basis set for atoms K through Zn. *J. Chem. Phys.* **1998**, *109* (4), 1223−1229.

(38) Rassolov, V. A.; Ratner, M. A.; Pople, J. A.; Redfern, P. C.; Curtiss, L. A. 6−31G* basis set for third-row atoms. *J. Comput. Chem.* **2001**, *22* (9), 976−984.

(39) Cossi, M.; Barone, V.; Cammi, R.; Tomasi, J. Ab initio study of solvated molecules: a new implementation of the polarizable continuum model. *Chem. Phys. Lett.* **1996**, *255* (4−6), 327−335.

(40) Miertuš, S.; Scrocco, E.; Tomasi, J. Electrostatic interaction of a solute with a continuum. A direct utilizaion of AB initio molecular potentials for the prevision of solvent effects. *Chem. Phys.* **1981**, *55* (1), 117−129.

(41) Kim, S.; Bolton, E. E. Pubchem: a large-scale public chemical database for drug discovery. *Open Access Databases and Datasets for Drug Discovery* **2024**, 39−66.

(42) Abraham, M.; Alekseenko, A.; Basov, V.; Bergh, C.; Briand, E.; Brown, A.; Doijade, M.; Fiorin, G.; Fleischmann, S.; Gorelov, S.;et al.*GROMACS 2024.2 Source code (2024.2)*; Zenodo, 2024.

(43) Jorgensen, W. L.; Maxwell, D. S.; Tirado-Rives, J. Development and testing of the OPLS all-atom force field on conformational energetics and properties of organic liquids. *J. Am. Chem. Soc.* **1996**, *118* (45), 11225−11236.

(44) Bernardes, C. E. S.; Joseph, A. Evaluation of the OPLS-AA force field for the study of structural and energetic aspects of molecular organic crystals. *J. Phys. Chem. A* **2015**, *119* (12), 3023−3034.

(45) Dodda, L. S.; Cabeza de Vaca, I.; Tirado-Rives, J.; Jorgensen, W. L. LigParGen web server: an automatic OPLS-AA parameter generator for organic ligands. *Nucleic Acids Res.* **2017**, *45* (W1), W331−W336.

(46) Lourenço, T. C.; Dias, L. G.; Da Silva, J. L. F. Theoretical investigation of the Na+ transport mechanism and the performance of ionic liquid-based electrolytes in sodium-ion batteries. *ACS Applied Energy Materials* **2021**, *4* (5), 4444−4458.

(47) Gouveia, A. S. L.; Bernardes, C. E. S.; Tomé, L. C.; Lozinskaya, E. I.; Vygodskii, Y. S.; Shaplov, A. S.; Lopes, J. N. C.; Marrucho, I. M. Ionic liquids with anions based on fluorosulfonyl derivatives: from asymmetrical substitutions to a consistent force field model. *Phys. Chem. Chem. Phys.* **2017**, *19* (43), 29617−29624.

(48) Martínez, L.; Andrade, R.; Birgin, E. G.; Martínez, J. M. PACKMOL: A package for building initial configurations for molecular dynamics simulations. *J. Comput. Chem.* **2009**, *30* (13), 2157−2164.

(49) Bussi, G.; Donadio, D.; Parrinello, M. Canonical sampling through velocity rescaling. *J. Chem. Phys.* **2007**, *126* (1), No. 014101.

(50) Berendsen, H. J. C.; Postma, J. P. M.; van Gunsteren, W. F.; DiNola, A.; Haak, J. R. Molecular dynamics with coupling to an external bath. *J. Chem. Phys.* **1984**, *81* (8), 3684−3690.

(51) Nosé, S. A unified formulation of the constant temperature molecular dynamics methods. *J. Chem. Phys.* **1984**, *81* (1), 511−519.

(52) Hoover, W. G. Canonical dynamics: Equilibrium phase-space distributions. *Phys. Rev. A* **1985**, *31* (3), 1695−1697.

(53) Parrinello, M.; Rahman, A. Polymorphic transitions in single crystals: A new molecular dynamics method. *J. Appl. Phys.* **1981**, *52* (12), 7182−7190.

(54) Hess, B.; Bekker, H.; Berendsen, H. J. C.; Fraaije, J. G. E. M. LINCS: A linear constraint solver for molecular simulations. *J. Comput. Chem.* **1997**, *18* (12), 1463−1472.

(55) Essmann, U.; Perera, L.; Berkowitz, M. L.; Darden, T.; Lee, H.; Pedersen, L. G. A smooth particle mesh Ewald method. *J. Chem. Phys.* **1995**, *103* (19), 8577−8593.

(56) Michaud-Agrawal, N.; Denning, E. J.; Woolf, T. B.; Beckstein, O. MDAnalysis: a toolkit for the analysis of molecular dynamics simulations. *J. Comput. Chem.* **2011**, *32* (10), 2319−2327.

(57) Gowers, R. J.; Linke, M.; Barnoud, J.; Reddy, T. J. E.; Melo, M. N.; Seyler, S. L.; Domanski, J.; Dotson, D. L.; Buchoux, S.; Kenney, I. M. *MDAnalysis: a Python package for the rapid analysis of molecular dynamics simulations*; Los Alamos National Laboratory (LANL), 2019.

(58) Savitzky, A.; Golay, M. J. E. Smoothing and differentiation of data by simplified least squares procedures. *Anal. Chem.* **1964**, *36* (8), 1627−1639.

(59) Li, K.; Galle Kankanamge, S. R.; Weldeghiorghis, T. K.; Jorn, R.; Kuroda, D. G.; Kumar, R. Predicting ion association in sodium electrolytes: A transferrable model for investigating glymes. *J. Phys. Chem. C* **2018**, *122* (9), 4747−4756.

(60) Liao, D. W.; Cho, T. H.; Sarna, S.; Jangid, M. K.; Kawakami, H.; Kotaka, T.; Aotani, K.; Dasgupta, N. P. Interfacial dynamics of carbon interlayers in anode-free solid-state batteries. *Journal of Materials Chemistry A* **2024**, *12* (10), 5990−6003.

(61) Kwabi, D. G.; Bryantsev, V. S.; Batcho, T. P.; Itkis, D. M.; Thompson, C. V.; Shao-Horn, Y. Experimental and computational analysis of the solvent-dependent $O_2/Li^+{-}O_2^-$ redox couple: Standard potentials, coupling strength, and implications for lithium−oxygen batteries. *Angew. Chem., Int. Ed.* **2016**, *55* (9), 3129−3134.

(62) Vitoriano, N. O.; De Larramendi, I. R.; Sacci, R. L.; Lozano, I.; Bridges, C. A.; Arcelus, O.; Enterría, M.; Carrasco, J.; Rojo, T.; Veith, G. Goldilocks and the three glymes: How Na^+ solvation controls $Na{-}O_2$ battery cycling. *Energy Storage Mater.* **2020**, *29*, 235−245.

(63) Ghasemiahangarani, P.; Farhan, G.; del Mundo, D.; Schoetz, T. Charge storage mechanisms in batteries and capacitors: A perspective of the electrochemical interface. *Adv. Energy Mater.* **2025**, *15* (12), No. 2404704.

(64) Klein, F.; Jache, B.; Bhide, A.; Adelhelm, P. Conversion reactions for sodium-ion batteries. *Phys. Chem. Chem. Phys.* **2013**, *15* (38), 15876−15887.

(65) Aurbach, D.; Daroux, M.; Faguy, P.; Yeager, E. The electrochemistry of noble metal electrodes in aprotic organic solvents containing lithium salts. *Journal of Electroanalytical Chemistry and Interfacial Electrochemistry* **1991**, *297* (1), 225−244.

(66) Mogensen, R.; Brandell, D.; Younesi, R. Solubility of the solid electrolyte interphase (SEI) in sodium ion batteries. *ACS Energy Letters* **2016**, *1* (6), 1173−1178.

(67) Ma, L. A.; Naylor, A. J.; Nyholm, L.; Younesi, R. Strategies for mitigating dissolution of solid electrolyte interphases in sodium-ion batteries. *Angew. Chem., Int. Ed.* **2021**, *60* (9), 4855−4863.

(68) Goren, E.; Chusid, O.; Aurbach, D. The application of in situ FTIR spectroscopy to the study of surface films formed on lithium and noble metals at low potentials in Li battery electrolytes. *J. Electrochem. Soc.* **1991**, *138* (5), L6.

(69) Machida, K.; Miyazawa, T. Infrared and Raman spectra of polyethyleneglycol dimethylethers in the liquid state. *Spectrochim. Acta* **1964**, *20* (12), 1865−1873.

(70) Parveen, S.; Sehrawat, P.; Hashmi, S. A. Triglyme-based solvate ionic liquid gelled in a polymer: A novel electrolyte composition for sodium ion battery. *Materials Today Communications* **2022**, *31*, No. 103392.

(71) Su, N.; Noor, S.; Roslee, M.; Mohamed, N.; Ahmad, A.; Yahya, M. Potential complexes of $NaCF_3SO_3$-tetraethylene dimethyl glycol ether (tetraglyme)-based electrolytes for sodium rechargeable battery application. *Ionics* **2019**, *25* (2), 541−549.

(72) Chandran, K.; Nithya, R.; Sankaran, K.; Gopalan, A.; Ganesan, V. Synthesis and characterization of sodium alkoxides. *Bulletin of Materials Science* **2006**, *29* (2), 173−179.

(73) Grdadolnik, J. ATR-FTIR spectroscopy: Its advantage and limitations. *Acta Chim. Slov.* **2002**, *49* (3), 631−642.

(74) Guo, L.; Thornton, D. B.; Koronfel, M. A.; Stephens, I. E. L.; Ryan, M. P. Degradation in lithium ion battery current collectors. *Journal of Physics: Energy* **2021**, *3* (3), No. 032015.

(75) Moulder, J. F.; Stickle, W. F.; Sobol, P. E.; Bomben, K. D. *Handbook of X-ray photoelectron spectroscopy: a reference book of standard spectra for identification and interpretation of XPS data*; Physical Electronics: Eden Prairie, MN, 1995.

(76) Fiedler, C.; Luerssen, B.; Rohnke, M.; Sann, J.; Janek, J. XPS and SIMS analysis of solid electrolyte interphases on lithium formed by ether-based electrolytes. *J. Electrochem. Soc.* **2017**, *164* (14), A3742.

(77) Zhang, J.; Wang, D.-W.; Lv, W.; Zhang, S.; Liang, Q.; Zheng, D.; Kang, F.; Yang, Q.-H. Achieving superb sodium storage performance on carbon anodes through an ether-derived solid electrolyte interphase. *Energy Environ. Sci.* **2017**, *10* (1), 370−376.

(78) Pan, J.; Sun, Y.-y.; Yan, Y.; Feng, L.; Zhang, Y.; Lin, A.; Huang, F.; Yang, J. Revisit electrolyte chemistry of hard carbon in ether for Na storage. *JACS Au* **2021**, *1* (8), 1208−1216.

(79) Jiang, K. S.; Hobold, G. M.; Guo, R.; Kim, K.-H.; Melemed, A. M.; Wang, D.; Zuin, L.; Gallant, B. M. Probing the functionality of LiFSI structural derivatives as additives for Li metal anodes. *ACS Energy Letters* **2022**, *7* (10), 3378−3385.

(80) Takeyoshi, J.; Kobori, N.; Kanamura, K. Electrochemical evaluation of lithium-metal anode in highly concentrated ethylene carbonate based electrolytes. *Electrochemistry* **2020**, *88* (6), 540−547.

(81) Wang, X.; Zhang, M.; Alvarado, J.; Wang, S.; Sina, M.; Lu, B.; Bouwer, J.; Xu, W.; Xiao, J.; Zhang, J.-G.; et al. New insights on the structure of electrochemically deposited lithium metal and its solid electrolyte interphases via cryogenic TEM. *Nano Lett.* **2017**, *17* (12), 7606−7612.

(82) Li, Y.; Li, Y.; Pei, A.; Yan, K.; Sun, Y.; Wu, C.-L.; Joubert, L.-M.; Chin, R.; Koh, A. L.; Yu, Y.; et al. Atomic structure of sensitive battery materials and interfaces revealed by cryo−electron microscopy. *Science* **2017**, *358* (6362), 506−510.

(83) Geysens, P.; Rangasamy, V. S.; Thayumanasundaram, S.; Robeyns, K.; Van Meervelt, L.; Locquet, J.-P.; Fransaer, J.; Binnemans, K. Solvation structure of sodium bis(fluorosulfonyl)-imide-glyme solvate ionic liquids and its influence on cycling of Na-MNC cathodes. *J. Phys. Chem. B* **2018**, *122* (1), 275−289.

(84) Zhang, C.; Ueno, K.; Yamazaki, A.; Yoshida, K.; Moon, H.; Mandai, T.; Umebayashi, Y.; Dokko, K.; Watanabe, M. Chelate effects in glyme/lithium bis (trifluoromethanesulfonyl) amide solvate ionic liquids. I. Stability of solvate cations and correlation with electrolyte properties. *J. Phys. Chem. B* **2014**, *118* (19), 5144−5153.

(85) Huang, W.; Frech, R.; Wheeler, R. A. Molecular structures and normal vibrations of trifluoromethane sulfonate ($CF_3SO_3^-$) and its lithium ion pairs and aggregates. *J. Phys. Chem.* **1994**, *98* (1), 100−110.

(86) Jiang, L.; Liu, L.; Yue, J.; Zhang, Q.; Zhou, A.; Borodin, O.; Suo, L.; Li, H.; Chen, L.; Xu, K.; et al. High-voltage aqueous Na-ion battery enabled by inert-cation-assisted water-in-salt electrolyte. *Adv. Mater.* **2020**, *32* (2), No. 1904427.

(87) Giffin, G. A.; Moretti, A.; Jeong, S.; Passerini, S. Complex nature of ionic coordination in magnesium ionic liquid-based electrolytes: Solvates with mobile Mg^{2+} cations. *J. Phys. Chem. C* **2014**, *118* (19), 9966−9973.

(88) Morales, D.; Ruther, R. E.; Nanda, J.; Greenbaum, S. Ion transport and association study of glyme-based electrolytes with lithium and sodium salts. *Electrochim. Acta* **2019**, *304*, 239−245.

(89) Gebala, A. E.; Jones, M. M. The acid catalyzed hydrolysis of hexafluorophosphate. *Journal of Inorganic and Nuclear Chemistry* **1969**, *31* (3), 771−776.

(90) Haartz, J. C.; McDaniel, D. H. Fluoride ion affinity of some Lewis acids. *J. Am. Chem. Soc.* **1973**, *95* (26), 8562−8565.

(91) Tasaki, K.; Kanda, K.; Nakamura, S.; Ue, M. Decomposition of $LiPF_6$ and stability of PF_5 in Li-ion battery electrolytes: Density functional theory and molecular dynamics studies. *J. Electrochem. Soc.* **2003**, *150* (12), A1628−A1636.

(92) Plakhotnyk, A. V.; Ernst, L.; Schmutzler, R. Hydrolysis in the system $LiPF_6$−propylene carbonate−dimethyl carbonate−H_2O. *J. Fluorine Chem.* **2005**, *126* (1), 27−31.

(93) Strmcnik, D.; Castelli, I. E.; Connell, J. G.; Haering, D.; Zorko, M.; Martins, P.; Lopes, P. P.; Genorio, B.; Østergaard, T.; Gasteiger, H. A.; et al. Electrocatalytic transformation of HF impurity to H_2 and LiF in lithium-ion batteries. *Nature Catalysis* **2018**, *1* (4), 255−262.

(94) Barnes, P.; Smith, K.; Parrish, R.; Jones, C.; Skinner, P.; Storch, E.; White, Q.; Deng, C.; Karsann, D.; Lau, M. L.; et al. A non-aqueous sodium hexafluorophosphate-based electrolyte degradation study: Formation and mitigation of hydrofluoric acid. *J. Power Sources* **2020**, *447*, No. 227363.

(95) Budi, A.; Basile, A.; Opletal, G.; Hollenkamp, A. F.; Best, A. S.; Rees, R. J.; Bhatt, A. I.; O'Mullane, A. P.; Russo, S. P. Study of the initial stage of solid electrolyte interphase formation upon chemical reaction of lithium metal and N-methyl-N-propyl-pyrrolidinium-bis(fluorosulfonyl)imide. *J. Phys. Chem. C* **2012**, *116* (37), 19789−19797.

(96) Shkrob, I. A.; Marin, T. W.; Zhu, Y.; Abraham, D. P. Why bis(fluorosulfonyl)imide is a "magic anion" for electrochemistry. *J. Phys. Chem. C* **2014**, *118* (34), 19661−19671.

(97) Galvez-Aranda, D. E.; Seminario, J. M. Li-metal node in dilute electrolyte LiFSI/TMP: Electrochemical stability using ab initio molecular dynamics. *J. Phys. Chem. C* **2020**, *124* (40), 21919−21934.

(98) Shkrob, I. A.; Marin, T. W.; Chemerisov, S. D.; Wishart, J. F. Radiation induced redox reactions and fragmentation of constituent ions in ionic liquids. 1. Anions. *J. Phys. Chem. B* **2011**, *115* (14), 3872−3888.

(99) Rajput, N. N.; Qu, X.; Sa, N.; Burrell, A. K.; Persson, K. A. The coupling between stability and ion pair formation in magnesium electrolytes from first-principles quantum mechanics and classical molecular dynamics. *J. Am. Chem. Soc.* **2015**, *137* (9), 3411−3420.

(100) Liu, Y.; Yu, P.; Wu, Y.; Yang, H.; Xie, M.; Huai, L.; Goddard, W. A.; Cheng, T. The DFT-ReaxFF hybrid reactive dynamics method with application to the reductive decomposition reaction of the TFSI and DOL electrolyte at a lithium−metal anode surface. *J. Phys. Chem. Lett.* **2021**, *12* (4), 1300−1306.

(101) Ko, S.; Obukata, T.; Shimada, T.; Takenaka, N.; Nakayama, M.; Yamada, A.; Yamada, Y. Electrode potential influences the reversibility of lithium-metal anodes. *Nature Energy* **2022**, *7* (12), 1217−1224.

(102) Melemed, A. M.; Skiba, D. A.; Gallant, B. M. Toggling calcium plating activity and reversibility through modulation of Ca^{2+} speciation in borohydride-based electrolytes. *J. Phys. Chem. C* **2022**, *126* (2), 892−902.

(103) Takida, H.; Kondo, Y.; Katayama, Y.; Hirata, K.; Yamashita, T.; Yamada, Y. ^{23}Na NMR chemical shift as a descriptor of sodium electrode potential. *J. Phys. Chem. C* **2026**, *130*, 4695.

(104) Seguin, T. J.; Hahn, N. T.; Zavadil, K. R.; Persson, K. A. Elucidating non-aqueous solvent stability and associated decomposition mechanisms for Mg energy storage applications from first-principles. *Front. Chem.* **2019**, *7*, 175.

(105) Bhattacharjee, S.; Isegawa, M.; Garcia-Ratés, M.; Neese, F.; Pantazis, D. A. Ionization energies and redox potentials of hydrated transition metal ions: evaluation of domain-based local pair natural orbital coupled cluster approaches. *J. Chem. Theory Comput.* **2022**, *18* (3), 1619−1632.

(106) Dooley, M. R.; Vyas, S. Role of explicit solvation and level of theory in predicting the aqueous reduction potential of carbonate radical anion by DFT. *Phys. Chem. Chem. Phys.* **2025**, *27* (14), 6867−6874.

(107) Yu, Y.; Baskin, A.; Valero-Vidal, C.; Hahn, N. T.; Liu, Q.; Zavadil, K. R.; Eichhorn, B. W.; Prendergast, D.; Crumlin, E. J. Instability at the electrode/electrolyte interface induced by hard cation chelation and nucleophilic attack. *Chem. Mater.* **2017**, *29* (19), 8504−8512.

(108) Busca, G. Chapter three - Structural, surface, and catalytic properties of aluminas. In *Adv. Catal.*, Jentoft, F. C. Ed.; Vol. *57*; Academic Press, 2014; pp 319−404.

(109) Mukhamed'yarova, A. N.; Gareev, B. I.; Nurgaliev, D. K.; Aliev, F. A.; Vakhin, A. V. A review on the role of amorphous aluminum compounds in catalysis: Avenues of investigation and potential application in petrochemistry and oil refining. *Processes* **2021**, *9* (10), 1811.

(110) Pu, J. K.; Viswanathan, V. Thermodynamic origin of Li underpotential and overpotential deposition on current collectors. *J. Phys. Chem. C* **2025**, *129* (16), 7677−7688.

(111) Sanchez, A. J.; Kazyak, E.; Chen, Y.; Chen, K.-H.; Pattison, E. R.; Dasgupta, N. P. Plan-view operando video microscopy of Li metal anodes: Identifying the coupled relationships among nucleation, morphology, and reversibility. *ACS Energy Letters* **2020**, *5* (3), 994−1004.

(112) Lin, D.; Liu, Y.; Li, Y.; Li, Y.; Pei, A.; Xie, J.; Huang, W.; Cui, Y. Fast galvanic lithium corrosion involving a Kirkendall-type mechanism. *Nat. Chem.* **2019**, *11* (4), 382−389.